Creep stability of the DART/Hera mission target 65803 Didymos: II. The role of cohesion

Yun Zhang [a,*], Patrick Michel [a], Derek C. Richardson [b], Olivier S. Barnouin [c], Harrison F. Agrusa [b], Kleomenis Tsiganis [d], Claudia Manzoni [e], Brian H. May [e]

[a] Université Côte d'Azur, Observatoire de la Côte d'Azur, CNRS, Laboratoire Lagrange, Nice 06304, France
[b] Department of Astronomy, University of Maryland, College Park, MD 20742, United States
[c] The Johns Hopkins University, Applied Physics Laboratory, United States
[d] Department of Physics, Aristotle University of Thessaloniki, Thessaloniki, Greece
[e] London Stereoscopic Company, London, United Kingdom

ABSTRACT

The binary asteroid 65803 Didymos-Dimorphos is the target of the first asteroid deflection test (NASA's Double Asteroid Redirection Test, DART) and the first binary asteroid system that will be characterized by a rendezvous mission (ESA's Hera). The cohesive strength of the fast-spin-primary Didymos is a key factor that could affect the impact outcome and stability of this system. To support the preparation and data interpretation of these missions and gain a better understanding of the formation and evolution of this system, we investigate the structural stability and cohesive strength of Didymos based on current observational information. We use the Didymos radar shape model to construct rubble-pile models consisting of ~40,000 to ~100,000 particles with different arrangements and size distributions. To investigate the effect of cohesion on the structural stability and dynamical behaviors of Didymos, we explicitly simulate the YORP spin-up process of these rubble-pile models from a slow spin state to Didymos' current spin state using a high-efficiency soft-sphere-discrete-element-model code, *pkdgrav*. We test the creep stability of Didymos' rubble-pile representation with different values of cohesion and derive the critical amount of cohesion to maintain stability. The results show that Didymos should at least have a minimum bulk cohesion on the order of 10 Pa to maintain its structural stability if the interparticle tensile strength is uniformly distributed. Since the surface particles are less bonded by cohesive contacts than the interior particles, the internal macroscopic cohesion is about three times the surface macroscopic cohesion. We find that the bulk density and particle arrangement and size distribution of Didymos have significant influences on its critical cohesion and failure behaviors, indicating different binary formation pathways. With the critical cohesion, Didymos is at the edge of maintaining a stable shape, and a rapid small decrease in its spin period would excite its rubble-pile structure and lead to reshaping or mass shedding. Whether the DART impact could partially or globally destabilize this system requires further investigation of the full two-body gravitational dynamics and the ejecta evolution. With the expected measurements returned by DART's onboard cubesat LICIACube in 2022 and Hera in 2027, the correlations between Didymos' physical properties and failure behaviors found in this study may be possible to constrain the mechanical properties and evolutionary history of this binary system.

1. Introduction

This paper is the second in a series of papers devoted to investigating the stability and physical properties of the binary asteroid (65803) Didymos-Dimorphos. This asteroid system is the target of the first asteroid deflection test involving NASA's DART (Cheng et al., 2018) and

ESA's Hera (Michel et al., 2018) missions, both being now approved by their respective agencies and in development for launch in 2021 and 2024, respectively. The Didymos-Dimorphos system also represents a special class of binary asteroids, whose primaries have top-shaped appearances and are at risk of rotational disruption (Ostro et al., 2006; Pravec and Harris, 2007; Pravec et al., 2010). The theory of YORP-

induced spin-up effects on asteroids could be a possible explanation for these remarkable characteristics (Scheeres, 2007; Walsh et al., 2008; Harris et al., 2009; Walsh and Jacobson, 2015), while the detailed dynamical processes and the complex dependencies on the physical properties are still poorly understood (Sánchez and Scheeres, 2012; Zhang et al., 2018; Ferrari and Tanga, 2020; Hirabayashi et al., 2020). To gain a better understanding of the formation and evolution of these binary systems as well as support the preparation and data interpretation of the DART and Hera missions, careful theoretical analyses and numerical explorations into the Didymos-Dimorphos system based on current observational information are required.

In the first paper (Zhang et al., 2017), hereafter referred to as paper I, we investigated the creep stability of the primary Didymos in the absence of Dimorphos, with an assumption that it is a cohesionless spinning self-gravitating aggregate (a rubble-pile structure is considered to be an appropriate model for most small asteroids; Richardson et al., 2002). By using a soft-sphere discrete element model (SSDEM) and a quasi-static spin-up procedure, we explicitly modeled the YORP rotational acceleration effect by spinning up the aggregate from an initial spin period of 5 hr to Didymos's current spin period of 2.26 hr. The simulation results show that the internal configuration (i.e., particle size and density distribution, and particle arrangement) and material parameters have strong influences on the structural stability and failure behaviors of a rubble-pile object. By monitoring the deformation, the surface mass movement, and the stress distribution during the spin-up process, and analyzing the creep stability, we were able to identify the critical spin limits of the simulated Didymos rubble-pile representations. We found that the rubble pile can be stable at a higher spin rate for a higher friction angle or a configuration with higher shear resistance. The cohesionless Didymos cannot remain geostatically stable with its nominal bulk density of ~2.1 g/cc. Nonetheless, for some very special internal configurations (i.e., a hexagonal close packing or a higher-density core), these rubble-pile representations can be marginally stable if their bulk densities are close to the maximum possible bulk density estimated from observations (i.e., ~2.4–2.5 g/cc).

However, it would be surprising if Didymos is a cohesionless rubble pile, given its rapid spin state and the fact that van der Waals cohesive forces between fine regolith grains could be strong on small bodies' surfaces (Scheeres et al., 2010; Gundlach and Blum, 2013). Moreover, the targets of NASA's OSIRIS-REx and JAXA's Hayabusa2 missions, namely (101955) Bennu and (162173) Ryugu, are both spinning top-shaped rubble piles (Lauretta et al., 2019; Watanabe et al., 2019), and non-zero level of cohesion are likely (but may not necessary) for both of them (Barnouin et al., 2019; Scheeres et al., 2019; Hirabayashi et al., 2020), despite their currently lower spin rates when compared to Didymos.

In this paper, we investigate the role of cohesion in the creep stability of Didymos, in the absence of Dimorphos (its potential influence will be investigated in the third paper of this series). Cohesion is a fundamental property that is significant for understanding observed behaviors of small asteroids and making predictions. In effect, whether cohesion is present or not makes a very big difference in the behavior of a small asteroid under various processes, such as YORP spin-up (Sánchez and Scheeres, 2016; Zhang et al., 2018), surface motions (Hartzell and Scheeres, 2011; Yu et al., 2018), impact cratering (Arakawa et al., 2020; Raducan et al., 2020), and tidal disruption (Holsapple and Michel, 2008; Zhang and Lin, 2020). Moreover, with the wide diversity of rubble-pile asteroids' properties (e.g., bulk density, packing configuration, spin rate, shape), the effect of cohesion is very complex and remains largely unknown (Walsh, 2018; Hestroffer et al., 2019), calling for further investigation.

Following a similar approach developed in paper I, we construct some granular aggregates with Didymos's radar shape model and use the SSDEM version of the *N*-body code *pkdgrav* to model the gravitational and contact forces between the components of the aggregates. Thanks to a recent implementation of a cohesive force model in *pkdgrav* (Zhang

et al., 2018), the contacts between the components can undergo a certain amount of tension. The shear resistance is then provided by both the frictional and cohesive forces, which could significantly improve the structural stability of the granular aggregates.

Our first objective is to estimate the minimum cohesive strength that is required to maintain the structural stability of Didymos at its current spin rate (hereafter, we call this the "critical cohesive strength" or "critical cohesion"). In the planetary science community, the concept of the cohesive strength, or simply cohesion, is commonly referred to the macroscopic cohesive strength defined by the Drucker-Prager yield criterion in the context of elastic-plastic theory for continuum media (Holsapple, 2007). This definition involves variables that cannot be clearly related to the interparticle contact characteristics at the microscopic scale. Inferring the macroscopic material quantities from the microscopic properties is an essential problem in granular material research (Lätzel et al., 2000). In order to quantitatively measure the critical cohesion of Didymos based on our simulation results, we design two stress/strength analysis approaches to derive the macroscopic cohesion of rubble-pile objects in this study. This allows us to make appropriate comparisons with the critical cohesion estimated from the continuum theory, and understand the differences between the discrete element modeling and the continuum theory.

Our second objective is to improve our understanding of the role of cohesion in the dynamical behaviors and failure conditions of Didymos and also to provide additional constraints to its physical properties. Since the influence of cohesion might be different depending on the internal configuration of the rubble pile and on the frictional effect (Sánchez and Scheeres, 2016; Zhang et al., 2018; Leisner et al., 2020; Hu et al., 2021), which are poorly known, we do a similar exercise as in paper I by considering different kinds of possible rubble-pile configurations with various angles of friction. So we can understand the relative influence of cohesion in each configuration and the effect of the particle distribution on the critical cohesion. Moreover, given that there are large observational uncertainties in the bulk density of Didymos, we investigate the influence of the bulk density within the possible range estimated from observations and deduce a relation between the critical cohesion and the bulk density.

Our ultimate objective is to support the data interpretation of the DART and Hera missions. After the kinetic impactor experiment performed in the fall of 2022, by the DART spacecraft on Dimorphos, the Hera spacecraft will perform a rendezvous with the Didymos-Dimorphos system in early 2027 for the full characterization of the impact outcome (Cheng et al., 2018; Michel et al., 2018). The planning tasks for Hera include imaging Didymos and Dimorphos, measuring their mass, shape, structure, and composition, as well as investigating the crater produced by DART (Michel et al., 2020). The combination of the observed surface characteristics and our modeling can allow inferring its actual structural properties, which will also shed light on possible binary formation scenarios. Furthermore, given the fast spin rate of Didymos, perturbations caused by the DART impact may also induce some observable modifications of its shape (Hirabayashi et al., 2019). We explore this possibility using our SSDEM modeling and provide constrains to the physical properties of Didymos accordingly.

The present paper is self-contained and can be understood without reading paper I. In the following, we first introduce our numerical modeling method and the stress/strength analysis approaches for rubble-pile bodies in Section 2. We then present our results for different possible rubble-pile representations of Didymos and reveal the relation between the critical cohesion and the bulk density in Section 3. Section 4 compares our predictions for the critical cohesion with those using the continuum approach, and discusses the possible physical properties of Didymos and the implications for the DART and Hera missions. Section 5 highlights the main findings of this study and suggests some interesting avenues for future research.
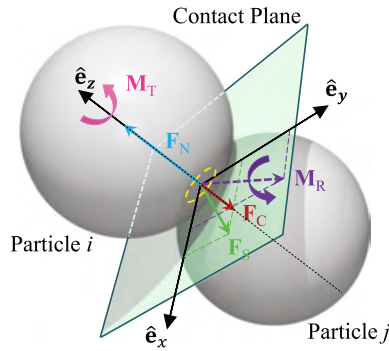
2. Methodology

2.1. Cohesive rubble pile modeling with SSDEM

We model Didymos as a self-gravitating rubble pile consisting of smaller spheres. In this rubble pile, each particle can interact with its surroundings through short-range forces (such as mechanical contact forces and van der Waals forces) and long-range forces (such as gravity and electrostatic forces[1]). We use the high-efficiency parallel *N*-body tree code, *pkdgrav* (Richardson et al., 2000; Stadel, 2001), and its implementation of the soft-sphere discrete element method (SSDEM) (Schwartz et al., 2012) to solve the contact interactions between particles in the rubble-pile model.

In the SSDEM, macroscopic particles are treated as deformable spheres, allowing overlaps between particles to act as proxies for actual deformation. Particles are taken to be in contact if and only if their surfaces are touching or mutually penetrating. The greater the extent of this penetration, the more repulsive a spring force that is generated to prevent further penetration. All contact forces and torques are then computed, accounting for static/dynamic tangential, as well as rolling and twisting frictions.

The SSDEM implementation has been presented in detail in Schwartz et al. (2012) and Zhang et al. (2017, 2018), and has been validated against various kinds of laboratory experiments therein. The reader might refer to Section 2 in Zhang et al. (2018) for the additional details about our soft-sphere granular physics contact model. Briefly, this model includes a linear spring-dashpot normal contact force, $\mathbf{F}_N$, a spring-dashpot-slider tangential contact force, $\mathbf{F}_S$, and two spring-dashpot-slider rotational torques in the rolling and twisting directions, $\mathbf{M}_R$ and $\mathbf{M}_T$. Fig. 1 shows a schematic of the directions of these forces and torques relative to the contact plane. The compressive strength of the interparticle contact is controlled by two stiffness constants, (k_N, k_S), for the normal and tangential directions. The contact energy dissipation is controlled by two coefficients of restitution, $(\varepsilon_N, \varepsilon_S)$, for the normal and tangential directions. The magnitude of contact friction is controlled by three friction coefficients for the tangential, rolling, and twisting directions, (μ_S, μ_R, μ_T). A shape parameter, β, first introduced in the contact model of Jiang et al. (2013, 2015), is designed to represent a

statistical measure of the effective contact area of realistic particle shapes (i.e., the yellow dashed circle in Fig. 1), which allows mimicking the strong rotational resistance and cohesive interactions between irregular particles.

With the assumption that there exist substantial micro-sized cohesive grains to cover larger boulders, meter-sized boulders that are connected through the interstitial grains (i.e., granular bridges) would be linked by cohesive interactions (Sánchez and Scheeres, 2014). The cumulative effect of the van der Waals cohesive forces of the fine grains between two large boulders can be modeled by a normal cohesive force and the associated frictional and rotational resistances without simulating each individual fine grain (Sánchez and Scheeres, 2016). Combining this granular bridge concept and the hypothetical effective contact area characterized by the shape parameter β, $A_{eff} = (2\beta r_{eff})^2$, the cohesive contact force along the normal direction in our model,

$$F_C = cA_{eff}, \tag{1}$$

where c is the interparticle tensile strength of this cohesive contact, the effective radius $r_{eff} = r_i r_j / (r_i + r_j)$, and r_i and r_j are the radii of the two particles in contact. As the magnitude of the rotational torques in our model are also proportional to A_{eff} (see Eq. (5) in Zhang et al., 2018), the strong rotational resistance due to the cohesive interstitial grains can be modeled in a consistent way. Therefore, although the behavior of individual interstitial grains is not physically simulated, our model can capture the resulting tensile strength and rotational resistances well, which is sufficient for our purpose of demonstrating the effect of cohesive strength on rubble-pile asteroids.

The cohesive force is added to the calculation of the contact interactions between two particles, and is ignored when the two particles are separated. Therefore, when the two particles are about to be separated with a low relative speed and their mutual penetration is negligible, the magnitude of the normal contact force $F_N \approx 0$ N. In this case, the contact between the two particles will break if the external force along the normal direction opposite to the cohesive force exceeds its magnitude F_C.

2.2. Quasi-static YORP effect modeling

The mechanical properties of granular materials depend on the loading history (Yasin and Tatsuoka, 2000; Luding, 2005), which is also true for our SSDEM simulations as the tangential force and the rotational torques in our contact model are history-dependent. In order to obtain reliable estimations on the material strengths, it is important to start an SSDEM simulation from a stress-free state and model the realistic stress history. For the purpose of this study, the Didymos rubble-pile representation should rotate at a slow spin rate initially and be spun-up by external effects up to Didymos' current spin rate.

The YORP effect resulting from the absorption and reemission of thermal radiation can exert torques on asteroids (Rubincam, 2000) and is the most ubiquitous mechanism to change their spin states (Vokrouhlický et al., 2003; Hergenrother et al., 2019). Driven by this effect, rubble-pile asteroids can be rotationally accelerated to their critical spin limits and reshape. Such processes could be responsible for the current rapid spin state of Didymos and the formation of Didymos-Dimorphos-like binary systems (Walsh and Jacobson, 2015). We artificially decrease the simulated rubble pile's spin period (i.e., adjust the velocity of the constituent particles accordingly) as a linear function of time to model the YORP effect. Paper I has verified that the stress state and the overall structure of a stable rubble pile are insensitive to the spin-up rate as long as the object is subject to quasi-static loading. Thus, we can use a

Fig. 1. Schematic of transmitted forces and torques acting on particle *i* through the contact with particle *j* (see the text for the definition of these forces and torques). $\hat{\mathbf{e}}_x$ and $\hat{\mathbf{e}}_y$ are in the contact plane and $\hat{\mathbf{e}}_z$ is in the normal direction according to the right-hand rule. The yellow dashed circle on the contact plane denotes the effective contact area of particle *i* and *j*. The figure is adapted from Fig. 1 in Zhang et al. (2017). (For interpretation of the references to color in this figure legend, the reader is referred to the web version of this article.)

---

[1] Since the electrostatic forces are not ubiquitous and the magnitude of asteroids' electric fields are largely uncertain (Scheeres et al., 2010; Hartzell, 2019), we assume that the particles are uncharged in this study.

spin-up rate much faster than the actual YORP effect in our simulations.[2] This treatment is appropriate for the purpose of testing the rubble pile's critical spin limit and failure behaviors, which are exactly the objectives of this study.[3] Only shortest-principal-axis rotation is considered in this study.

The spin-up procedure of our simulations consists of three spin-control stages, i.e., a fast spin-up stage, a slow spin-up stage, and a spin-maintain stage, as well as a free-evolution stage. Firstly, the simulated rubble pile, which has settled down under its self-gravity at the starting spin period T_{start}, is rapidly spun up to an intermediate spin period T_{inter} that is sufficiently larger than its failure spin period. Then, the spin period is decreased to T_{final} in a slower manner to ensure that the rubble pile stays in quasi-equilibrium states before structural failure occurs. After achieving T_{final}, the rubble pile is forced to keep this spin period. Pronounced structural failure of the rubble pile is diagnosed as having a reduction in its short-to-long axis ratio by 1% of the initial value. When this is identified at any step of the spin-up or spin-maintain process, we stop controlling the spin period of the simulated body and let it evolve freely under its own gravity (see the top frame in Fig. 2(a) for an example).

This spin-up procedure is similar to the one used in paper I. We adopted the same spin period parameters, i.e., $T_{start} = 5$ hr, $T_{inter} = 3$ hr, and $T_{final} = 2.26$ hr (i.e., the current spin period of Didymos). The simulation time to go from T_{start} to T_{inter} is 7000 s and from T_{inter} to T_{final} is 140,000 s. The inertial number $\ll 10^{-2}$ in this case, thus ensuring that the spin-up process is quasi-static (Koval et al., 2009). Given that the dynamical time for a rubble pile is $1/\sqrt{G\rho_B}$, i.e., ~2500 s for the case of Didymos, the rubble pile has sufficient time to response to the quasi-static loading and the simulations remain computationally expedient.

2.3. Two approaches to estimate the macroscopic cohesive strength of a rubble pile

The cohesive forces calculated by Eq. (1) only provide the tensile strength between two particles, while the macroscopic material strength of a rubble pile is defined in the sense of continuum medium, which is the cumulative effect of interparticle interactions in a representative element (Holsapple, 2007). Given the inhomogeneous, disordered, and anisotropic characteristics on microscopic scale in a rubble pile, we need to develop an averaging formalism to translate the microscopic information to macroscopic quantities. Here we design two approaches to quantify the possible range of the macroscopic material strengths of the simulated rubble pile.

2.3.1. Drucker–Prager yield criterion

First, we need to define the yield condition of granular material for performing our strength analyses. The macroscopic cohesion C technically means the value of the macroscopic shear strength at zero pressure. This is usually described by the Mohr-Coulomb yield criterion, or its smooth version, the Drucker-Prager yield criterion (i.e., in the stress space, the Drucker-Prager failure cone is taken to be circumscribed to the Mohr-Coulomb hexagonal pyramid; see Jaeger et al., 2009), which is written as[4]

$$\sqrt{J_2} \leq k + sI_1, \tag{2}$$

where I_1 is the first invariant of the Cauchy stress tensor and J_2 is the second invariant of the deviatoric stress tensor, which can be written in terms of the principal stresses, σ_1, σ_2, and σ_3 (from largest to smallest), as $I_1 = \sigma_1 + \sigma_2 + \sigma_3$, $J_2 = [(\sigma_1 - \sigma_2)^2 + (\sigma_2 - \sigma_3)^2 + (\sigma_3 - \sigma_1)^2]/6$. The material constants s and k can be expressed as a function of the commonly-used friction angle ϕ and the cohesive strength C,

$$s = \frac{2\sin\phi}{\sqrt{3}(3 - \sin\phi)}, \quad k = \frac{6C\cos\phi}{\sqrt{3}(3 - \sin\phi)}. \tag{3}$$

Eq. (2) with the equality defines the yield condition of granular material.

2.3.2. Maximum possible cohesive strength

The pioneer study of Rumpf (1958) has related the tensile strength of a coheisve granular assembly to its microstructure and the interparticle cohesive force as

$$\sigma_T \approx \frac{F_C N_{cont} \eta}{4\pi (r_{part})^2}, \tag{4}$$

where N_{cont} is the coordination number that describes the average number of contacts on each particle, η is the packing efficiency that corresponds to the fraction of the volume of the granular assembly filled by particles (the remaining fraction being defined as the porosity), and r_{part} is the particles radius.

This tensile strength measures the isotropic tensile stress assuming that all the contacts break at the yield threshold, i.e., $\sigma_1 = \sigma_2 = \sigma_3 = -\sigma_T$ (Molerus, 1975). In reality, the contacts of particles in a granular assembly do not all break simultaneously when the yield condition is met and therefore, Eq. (4) gives a maximum possible estimate on the isotropic tensile strength. Combining with the Drucker-Prager yield criterion (Eq. (2)), we define the following expression to calculate the maximum possible macroscopic cohesion C_{max} of a rubble pile,

$$C_{max} = \sigma_T \tan\phi. \tag{5}$$

For equal-sized particles in contact, the effective radius $r_{eff} = r_{part}/2$, and

$$C_{max} = \frac{c\beta^2 N_{cont} \eta \tan\phi}{4\pi}. \tag{6}$$

The average contact number N_{cont} can be obtained by dividing the total contact number by the total particle number. The friction angle ϕ can be evaluated based on the stress distribution discussed in Section 2.3.3. There are several ways to define the packing efficiency η of a rubble pile. For the maximum possible macroscopic cohesion estimate, we use the definition of the internal packing efficiency, which can be measured based on the Voronoi tessellation of this rubble pile (see Section 3.2 in Zhang et al., 2017, for details),

$$\eta_{inter} = \frac{1}{N_{inter}} \sum_{i=1}^{N_{inter}} \frac{4\pi r_i^3}{3V_i}, \tag{7}$$

where r_i is the radius and V_i is the volume of the Voronoi cell for the i-th particle, and N_{inter} is the number of particles in the interior of the rubble pile. We use the open-source library, $Voro++$ (Rycroft, 2009), to build the Voronoi tessellation of the rubble pile.

2.3.3. Minimum possible cohesive strength

In addition to the isotropic tensile failure, a rubble pile could have many kinds of failure modes (Hirabayashi, 2015; Sánchez and Scheeres, 2016; Zhang et al., 2018). The stress states in a rotating rubble pile would significantly change with the material parameters and the spin states (Zhang et al., 2018; Hirabayashi et al., 2020). A more accurate

---

[2] The characteristic YORP timescale for a km-sized asteroid to double its spin rate is normally above 1 Myr. A real-time simulation is well beyond the current computational power.

[3] As the YORP effect is sensitive to small-scale topographical changes (Statler, 2009; Cotto-Figueroa et al., 2015), the coupled effect of the shape and the YORP torque should be considered to predict the evolution of the rubble pile after structural failure, which will be investigated in our future research.

[4] In rock and soil mechanics, the compressive stress is expressed as a positive value, and the tensile stress is expressed as a negative value. We follow this convention in the expression of stress variables.

estimate on its cohesive strength requires that we evaluate the stress distribution at the moment of structural failure initiation.

The stress distribution analyses are carried out on the scale of representative volume elements (RVEs; see Section 3.3.1 in Zhang et al., 2017, and references therein for details). The size of a RVE is often taken to be about 12 times the radius of the typical particle for stress analyses (Masson and Martinez, 2000). We use a tree code to divide the rubble-pile body into several similar-sized subassemblies, i.e., RVEs. Each RVE contains about 200 to 300 particles. The average stress tensor of a local region, e.g., the j-th RVE, in a rubble pile can be assessed by averaging the stress tensor for every particle in this RVE,

$$\overline{\sigma}_j^{\mathrm{RVE}} = \frac{1}{V_j^{\mathrm{RVE}}} \sum_{i=1}^{N_j^{\mathrm{RVE}}} V_i \sigma_i = \frac{1}{V_j^{\mathrm{RVE}}} \sum_{i=1}^{N_j^{\mathrm{RVE}}} \sum_{k=1}^{N_{\mathrm{cont},i}} \mathbf{x}^{i,k} \otimes \mathbf{f}^{i,k}, \tag{8}$$

where N_j^{RVE} is the number of particles in this RVE and V_j^{RVE} is the total volume of this RVE. The Cauchy stress tensor σ_i for a single particle i is given as the summation of the dyadic product of the branch vector $\mathbf{x}^{i,k}$ that connects the particle center with the contact point and the corresponding contact force $\mathbf{f}^{i,k}$ for the k-th contact. $N_{\mathrm{cont},i}$ is the number of contacts for the i-th particle. The first invariant of the average stress tensor $I_{1,j}^{\mathrm{RVE}}$ and the second invariant of the deviatoric stress tensor $J_{2,j}^{\mathrm{RVE}}$ for the j-th RVE can be then determined from the average stress tensor $\overline{\sigma}_j^{\mathrm{RVE}}$.

The material parameters, i.e., the friction angle ϕ and the cohesive strength C, can be thus evaluated from the stress-state variables at the time of failure initiation. Our previous study shows that the value of the friction angle ϕ is independent of the cohesion (Zhang et al., 2018). So ϕ can be estimated by spin-up simulations with the same setup but $c = 0$ Pa. Then, for a cohesive rubble pile, if ϕ is known, the minimum required cohesion to keep a local region stable can be given by

$$C_{\min}^{\mathrm{RVE}} = \sqrt{3 J_{2,j}^{\mathrm{RVE}}} \frac{(3 - sin\phi)}{6 cos\phi} - I_{1,j}^{\mathrm{RVE}} \frac{tan\phi}{3}. \tag{9}$$

When the minimum required cohesion of a local region exceeds the actual cohesion of this rubble pile, this region starts to fail. Therefore, at the moment of failure initiation, the cohesion of the rubble pile can be estimated by

$$C_{\min} = \max_{0 \leq j \leq N_{\mathrm{RVE}}} \left. C_{\min}^{\mathrm{RVE}} \right|_{\mathrm{failure}}, \tag{10}$$

where N_{RVE} is the total number of RVEs of this rubble pile. The minimum required cohesive strength is essentially 0 Pa, i.e., no cohesion is needed, when the above estimate gives a negative value.

The subscript "min" in $C_{\min}$ marks that it estimates the minimum possible macroscopic cohesion. This is because there would only be a few contacts exceeding the interparticle tensile or shear strength in the failure RVE, while the other contacts could still be maintained. The shear stress averaged over this RVE could be smaller than the actual shear stress the local yield region might experience. $C_{\min}$ denotes the lower tensile/shear limit this RVE can withstand. In practice, we indeed find that the value of $C_{\min}$ slightly increases if a smaller RVE is used for the stress analyses (e.g., $C_{\min}$ increases from 5.4 Pa to 6.3 Pa if using smaller RVEs with ~50 particles in the case of a hexagonal packing; the friction angle is insensitive to the size of RVEs). However, considering the effect of large fluctuations of contact forces in the critical stage, the size of RVEs cannot be too small; otherwise, the stress analyses are unreliable (Masson and Martinez, 2000; Luding, 2005). Therefore, using RVEs with 200 to 300 particles to estimate the minimum possible macroscopic cohesion is appropriate.

3. Critical cohesion and failure behaviors of Didymos

In this section, we perform a series of spin-up simulations for six different Didymos rubble-pile models with various cohesion and bulk densities to explore the failure conditions and behaviors of Didymos. The critical cohesion of each rubble-pile model will be revealed.

3.1. Dynamical and physical properties of 65803 Didymos

Ground-based radars have been used to constrain some important properties of Didymos system, which are present in the recent paper by Naidu et al. (2020).[5] Table 1 presents the currently estimated main properties of Didymos. Since we ignore Dimorphos (the secondary) in this study, we just present here the properties of Didymos (the primary) that are relevant for our study. The Dynamically Equivalent Equal Volume Ellipsoid (DEEVE) is an ellipsoid with a uniform density and the same volume and moments of inertia as Didymos' shape model. The properties of this DEEVE are used in the continuum approach to analyze Didymos' critical cohesion (see Section 4.1). Among the main properties, the one with the biggest uncertainty is the size and, accordingly, the bulk density. In the following, we first study the behavior of Didymos with its nominal bulk density of 2170 kg/m^3 (called hereafter the "nominal Didymos") and then investigate the influence of the bulk density within its range of uncertainty.

3.2. Rubble-pile internal configuration and parameter setup

The internal configuration of rubble-pile objects is poorly known but plays an important role in their dynamical evolution (e.g., Zhang and Michel, 2020). Paper I showed that spin limits and failure behaviors are sensitive to the particle size distribution and arrangement in a rubble pile, which could also be important when cohesion is present.

To investigate this effect, we construct four kinds of Didymos rubble-pile packings based on the Didymos radar shape model, i.e., a hexagonal close packing (HCP), a monodisperse random close packing (RCP), and two dense polydisperse packing models with different particle size distribution (PP1 & PP2). The particle size in the HCP and RCP models is ~10 m. The PP1 case considers a range from ~4 to ~32 m, while the PP2 case considers a range from ~4 to ~16 m. The differential size distribution of the polydisperse models are assumed to follow a power law with an exponent of −3, close to the boulder size distribution observed on the surfaces of several asteroids (e.g., Michikami et al., 2010; Walsh et al., 2019; Michikami et al., 2019). Additionally, to test the effect of particle resolution on the critical cohesion estimation, we consider two extra polydisperse packing, PP3 & PP4, which have the same maximum-to-minimum particle size ratio and power law exponent as PP2 but with larger particles. The distribution of particles is homogeneous on the macroscopic scale in these models. Given that the resolution of the shape model is ~50 m, aggregates composed of decameter-sized particles are sufficient to match the shape. Reader

Table 1
Basic physical properties of Didymos (refer to Naidu et al., 2020). The mass of Didymos is derived from the size ratio with respect to Dimorphos and the total system mass (i.e., $(5.37 \pm 0.44) \times 10^{11}$ kg), under the assumption of equal density.

Parameters		Values
DEEVE extents along three principal axes (m)	a_1	797 ± 6%
	a_2	783 ± 6%
	a_3	761 ± 10%
Mass (kg)	M	$(5.32 \pm 0.43) \times 10^{11}$
Bulk density (kg/m^3)	ρ_B	2170 ± 350
Rotation period (hr)	T	2.2600 ± 0.0001

---

[5] Note that according to the updated observational data, the values summarized in Table 1 is slightly different from the Didymos properties used in Paper I (see Table 1 therein).

might refer to Section 2.3.3 in paper I for the detailed procedure to build a rubble pile with Didymos's shape. Although interstitial fine grains are not explicitly simulated in these rubble-pile models, their cumulative cohesion and friction effects on the meter-sized boulders can be well captured by our soft-sphere contact model (see Section 2.1).

Table 2 summarizes the physical properties of these rubble-pile models. Since the Didymos shape model is slightly different from the one used in paper I, the values of these properties are also slightly varied. To be consistent with the bulk density estimation approach for Didymos (Naidu et al., 2020), we calculate a rubble-pile model's bulk density ρ_B by dividing its mass by the volume of its DEEVE. Then the bulk packing efficiency η_B can be estimated by dividing ρ_B by the particle density ρ_{part}. Due to the boundary effect and larger voids on the surface, the internal packing efficiency η_{inter} calculated by Eq. (7) is always larger than η_B.[6]

The material parameters used in our contact model can be then assigned for each rubble-pile model according to the approach introduced in Schwartz et al. (2012) and Zhang et al. (2018). Briefly, The normal stiffness k_N and the timestep Δt are set to ensure that particle overlaps for each entire simulation do not exceed 1% of the radius of the minimum particle. The tangential stiffness k_S is set to $(2/7)k_N$ to keep normal and tangential oscillation frequencies equal to each other. The coefficients of restitution, ε_N and ε_S, are set to 0.55, resembling the energy dissipation behavior of terrestrial rocks (Chau et al., 2002). The four parameters, $(\mu_S, \mu_R, \mu_T, \beta)$, that give rise to shear strength are set to, (1.0, 1.05, 1.3, 0.5), corresponding to sand particles of medium hardness and frictional resistance (the same values as the nominal case used in paper I). The interparticle tensile strength c is the free parameter we need to explore to find the critical cohesion for the Didymos representations. These contact parameters are constant throughout a rubble pile.

3.3. Results for the nominal Didymos

We explore a vast range of c to test the creep stability of our six rubble-pile models in the spin-up process and determine the minimum value of c required to maintain their structure. We start the spin-up simulation with an initial c estimated for each rubble-pile model based on Eq. (6) and the continuum theory (see Holsapple, 2007, for the method of using the continuum theory to derive the bulk critical cohesion for rubble piles), and then decrease/increase c by 10 Pa if this body can/cannot be stable at the end of the spin-up process and restart the spin-up simulation. In this way, the interparticle critical cohesive strength c_{crit} is refined to the accuracy of 10 Pa. The subscript "crit" denotes that this variable corresponds to the property of a rubble pile that can be marginally stable at Didymos' fast spin state.

Fig. 2 presents the evolution of the shape, internal packing, and contact network characteristics during the spin-up process with the critical value of c for the HCP, RCP, PP1, and PP2 models, respectively. Two additional cases with smaller values of c are shown for comparison. The spin period T is evaluated based on the moment of inertia and the angular momentum of the whole particle system relative to the center of mass. Reshaping (changes in a_3/a_1), internal deformation (changes in

---

[6] Note that only particles with distances to the mass center smaller than 300 m is considered in the internal packing efficiency η_{inter} measurement in this study. This treatment is different from that used in paper I, in which the surface particles are excluded based on the size of their Voronoi cells. The latter treatment is biased toward smaller Voronoi cells, especially for polydisperse packings. Therefore, the values of the internal packing efficiency are different from those shown in paper I (see their Table 3). Nonetheless, since η_{inter} is only used to evaluate the internal deformation based on its variation and the absolute value of η_{inter} is irrelevant in paper I, the difference does not affect the results and conclusions in paper I. Since the approach for calculating the bulk density ρ_B is consistent with that used in paper I, we will see later that their estimates on the critical bulk density are consistent with the results of this study.

η_{inter}), and contact breakages (changes in N_{cont} and N_{cont}^1) can be observed during the spin-up process. As expected, an increase in the interparticle cohesion can postpone the initiation of failure and keep the structure stable at a faster spin state. Nonetheless, it is very interesting to note that a small variation in c could lead to dramatically different results. As indicated by Eq. (6) and our previous studies (e.g., Zhang et al., 2018), the macroscopic cohesive strength C is on the order of 1% to 10% of the interparticle tensile strength c in the case of $\beta = 0.5$. That is, a difference of 10 Pa in c means a small difference $\lesssim 1$ Pa in C, showing that the structural stability of a fast-rotating rubble pile is very sensitive to the cohesive strength. On the other hand, this sensitivity could help us to obtain a relative accurate estimate on the critical cohesion C_{crit} of Didymos. According to Eqs. (4) and (6), the indirect measuring error for $\sigma_{T, crit}$ and $C_{max, crit}$ is on the order of 1 Pa.

Table 3 summarizes the macroscopic cohesive strength of the six Didymos rubble-pile models with their respective c_{crit}. The critical tensile strength $\sigma_{T, crit}$ and the maximum critical cohesive strength $C_{max, crit}$ are evaluated according to Eqs. (4) and (6), respectively. The rubble-pile properties at the end state of the spin-up process (where the spin period $T = 2.26$ hr) are used in the evaluations.

The minimum critical cohesive strength $C_{min, crit}$ is evaluated based on the stress analyses. Fig. 3 presents the minimum required cohesion to keep each RVE stable during the spin-up process for different rubble-pile models. It is clear to see that C_{min}^{RVE} increases with the spin rate for most RVEs in a rubble pile. The actual cohesion of a local region should be larger than C_{min}^{RVE} to maintain its stability. We further spin up each rubble-pile model slightly from the stable state at $T = 2.26$ hr to induce structural failure, and then calculate $C_{min, crit}$ by Eq. (10). The actual spin limits of these rubble piles with their respective c_{crit} are in the range of 2.257–2.259 hr, which is very close to the spin period of Didymos. Therefore, their respective macroscopic strength can be regarded as the critical strength of Didymos in the case of their corresponding rubble-pile configuration.

There are notable differences between the values of the maximum and the minimum critical cohesive strength, i.e., $C_{max, crit}$ and $C_{min, crit}$. The former one is about three times as large as the latter one. The main reason is that, in a cohesive rubble pile with a constant interparticle cohesion, the failure-initiation region used to evaluate C_{min} is located at the surface area, as shown in Fig. 3. C_{min} in fact represents the surface cohesion. As the parameters used to evaluate C_{max} are defined on the global scale of a rubble pile, C_{max} represents the bulk cohesion. The local packing efficiency and coordination number of the surface particles are much lower than those of the interior particles. Therefore, the local macroscopic cohesive strength could be much smaller in the surface region, leading to the large differences between $C_{max, crit}$ and $C_{min, crit}$. In addition, the isotropic tensile failure mode assumed in the calculation of C_{max} could be different from the actual failure mode indicated by C_{min}. The size of RVEs could introduce some variations in the estimate of C_{min} as discussed in Section 2.3.3. These two possibilities may also contribute to the differences.

Another notable thing is the differences in the critical strength of different rubble-pile models. The failure behaviors shown in Fig. 2 and the associated animations are also very different. In the following, we analyze the characteristics of each rubble-pile model during the spin-up process and reveal the causes for these differences.

3.3.1. Hexagonal-closest-packing configuration (HCP)

A perfect hexagonal close packing would have a coordination number close to 12, which is the highest possible coordination number for a dry granular assembly made of spheres. Due to its compact contact network and particle interlocking, the HCP model has a friction angle as high as 43° and can maintain its stability at $T = 2.26$ hr with the smallest c_{crit} of 130 Pa (see Table 2).

Fig. 4 illustrates the distribution of the stress-state variables and the contact networks over a cross-section of the HCP structure at different spin periods. The contact networks are colored by the magnitude of the

Table 2

Physical properties of the Didymos rubble-pile models with the nominal bulk density of 2170 kg/m^3. N is the total number of particles, r_{part} is the particle radius, and ρ_{part} is the particle density. The interparticle critical tensile strength c_{crit} are obtained from our SSDEM simulations (see Section 3.3). The initial internal packing efficiency $\eta_{inter, 0}$, the initial bulk packing efficiency $\eta_{B, 0}$, the initial number of particles in contact with only one other particle $N^1_{cont,0}$, and the initial coordination number $N_{cont, 0}$, are measured based on each rubble pile with its critical cohesion at the beginning of the corresponding simulation. $N^1_{cont,end}$ and $N_{cont, end}$ describe the contact number at the end of the same simulation where the rubble pile is stable at the spin period of 2.26 hr.

Model	N	r_{part} (m)	ρ_{part} (kg/m^3)	c_{crit} (Pa)	$\eta_{inter, 0}$	$\eta_{B, 0}$	$N^1_{cont,0}$	$N^1_{cont,end}$	$N_{cont, 0}$	$N_{cont, end}$
HCP	45938	9.8	2956	130	0.741	0.734	0	0	11.357	9.725
RCP	39876	9.8	3413	350	0.641	0.636	24	30	5.239	4.299
PP1	52163	3.9–31.2	2997	370	0.732	0.724	677	1530	4.429	3.901
PP2	104516	3.9–15.6	3196	330	0.685	0.679	479	956	5.374	4.421
PP3	13049	7.8–31.2	3203	320	0.685	0.678	21	75	5.349	4.616
PP4	1562	15.5–62.0	3246	330	0.685	0.668	0	5	5.327	4.681
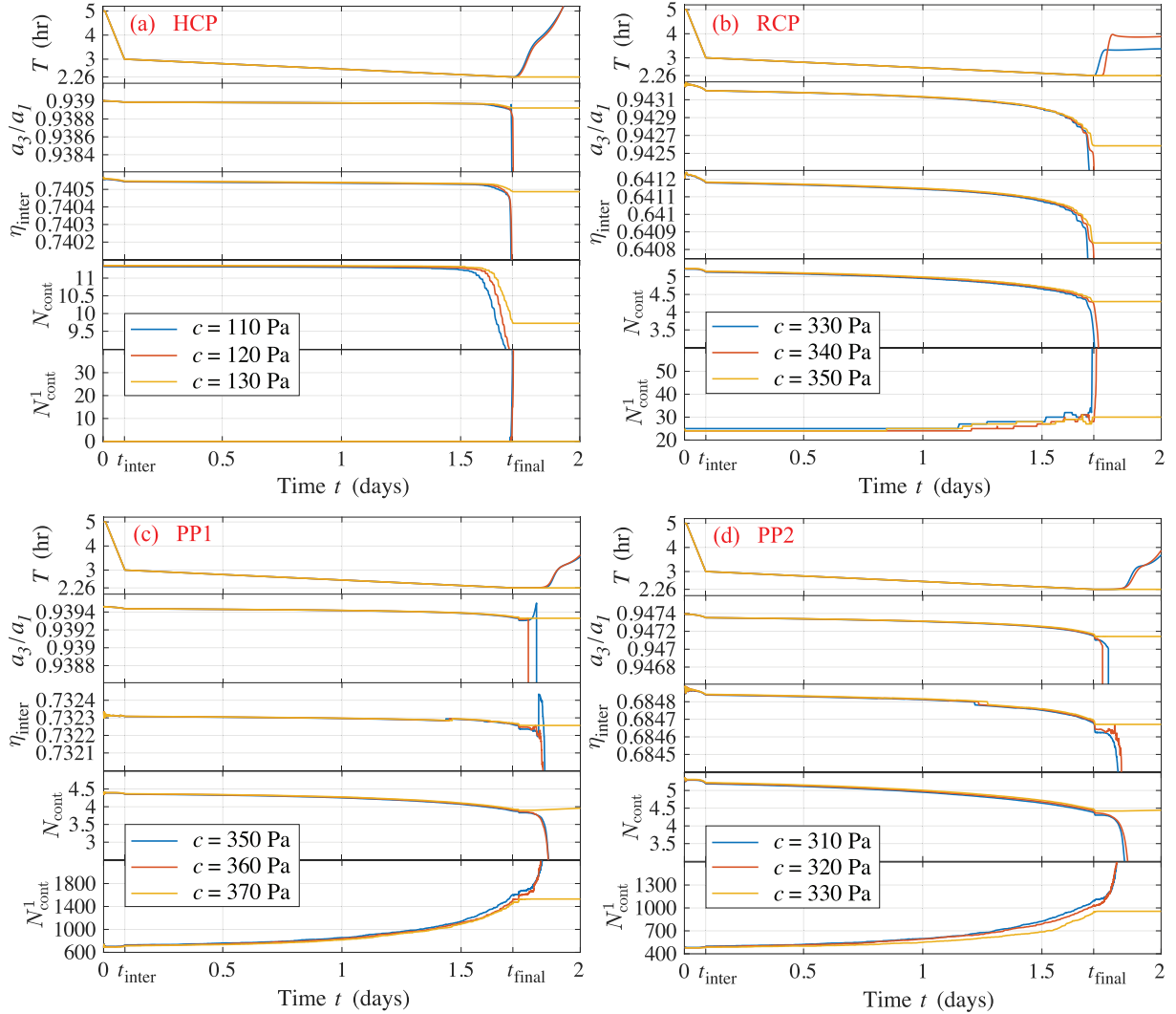
Fig. 2. Evolution of spin period (T, top frame), shortest-to-longest axis ratio (a_3/a_1, upper middle frame), internal packing efficiency (η_{inter}, middle frame), coordination number (N_{cont}, lower middle frame), and particle number with only one contact (N^1_{cont}, bottom frame) during spin-up processes for the HCP (a), RCP (b), PP1 (c), and PP2 (d) models. The results for different c are denoted in different colors as indicated in each legend (animations of the sub-critical cases, i.e., $c = 120$ Pa, 340 Pa, 360 Pa, and 320 Pa, for the four models, respectively, are available online).

normal contact strength, S_N, i.e., the total normal contact force divided by the effective contact area, so that the contacts that reach the cohesion limit (i.e., the given value of the interparticle tensile strength c used in the simulation) can be revealed.

The distribution of the pressure and shear stress are symmetric about the spin axis and most of the force chains are compressive at the slow spin state. As the spin rate increases, force chains near the equator

perpendicular to the spin-axis become tensile resisting the centrifugal force caused by the rapid rotation. These tensile force chains gradually spread to the pole region during the spin-up process. Eventually, cracks are initiated in the center region where interparticle cohesion allows for the formation of particle agglomerates. As shown in Fig. 4, the external particles are well connected to the particles in the sub-surface, leading to the formation of these large particle agglomerates. The centrifugal

Table 3
Macroscopic critical strength estimates of the Didymos rubble-pile models with the nominal bulk density of 2170 kg/m^3.

Model	ϕ (°)	$\sigma_{T, crit}$ (Pa)	$C_{max, crit}$ (Pa)	$C_{min, crit}$ (Pa)
HCP	43	18.6	17.4	5.4
RCP	30	19.2	11.1	2.4
PP1	39	21.0	17.0	4.3
PP2	38	19.9	15.5	4.5
PP3	38	20.1	15.7	2.7
PP4	38	21.1	16.5	−1.6

forces acting on the surface particles will also pull the sub-surface particles outward. And then the surface and sub-surface particles work together to pull the more internal particles until the cumulative centrifugal forces can be balanced by the summation of gravitational and cohesive forces or a crack occurs to cut off the agglomeration. Given the compact connection of the HCP model, the agglomeration behavior can propagate to the central region, causing crack initiation in the center. Along with the agglomeration process, most of the particles move outward, leading to volumetric dilation and crack growth in the radial direction that can extend to the surface. Due to the asymmetric Didymos shape model, this cracking process is nonuniform and results in a nonuniform stress distribution, as shown in the third column of Fig. 4.

The contact breakage and volumetric dilation behaviors are also observable in Fig. 2(a). When the HCP model is spun up to $T = 2.35$ hr, the coordination number N_{cont} begins to decrease as a results of the contact breakage. The internal packing efficiency η_{inter} and the axis ratio

a_3/a_1 then decrease at almost the same time, showing the behavior of volumetric dilation. As the structure is weakened by additional crack growth during the spin-up process, the asteroid may become heavily damaged. However, because of the high friction angle, the interlocking between the individual particles, and the formation of the particle agglomerates, the HCP rubble pile may remain stable. As shown in the case of $c = 130$ Pa in Fig. 2(a), the contact breakage and volumetric dilation behaviors cease as soon as spin-up ends. The HCP model is stable at $T = 2.26$ hr with a coordination number of 9.725, a number that is significantly smaller than what it began with. For the case of $c = 120$ Pa, the contact breakage cannot be stopped at the final spin rate. The surface agglomerates move outward, leading to large deformation of the whole rubble pile (see the supplementary video of the HCP model).

3.3.2. Monodisperse random-close-packing configuration (RCP)

The RCP model has the same particle size distribution as the HCP model but with different arrangement. Its random configuration results in a lower packing efficiency, a smaller coordination number, and a lower friction angle (30°). Accordingly, its interparticle critical tensile strength $c_{crit} = 350$ Pa, which is much larger than that of the HCP model. However, the bulk critical tensile strength $\sigma_{T, crit}$ is similar for these two models as the difference in c_{crit} is compensated by the differences in the coordination number and the packing efficiency (see Table 3; in fact, the relation between the rubble-pile packing and the value of $\sigma_{T, crit}$ also has a complicated dependency on the failure modes, as present in Section 3.4 below). Since the cohesive strength is an increasing function of the friction angle (i.e., Eq. (5)), the bulk critical cohesive strength of the RCP
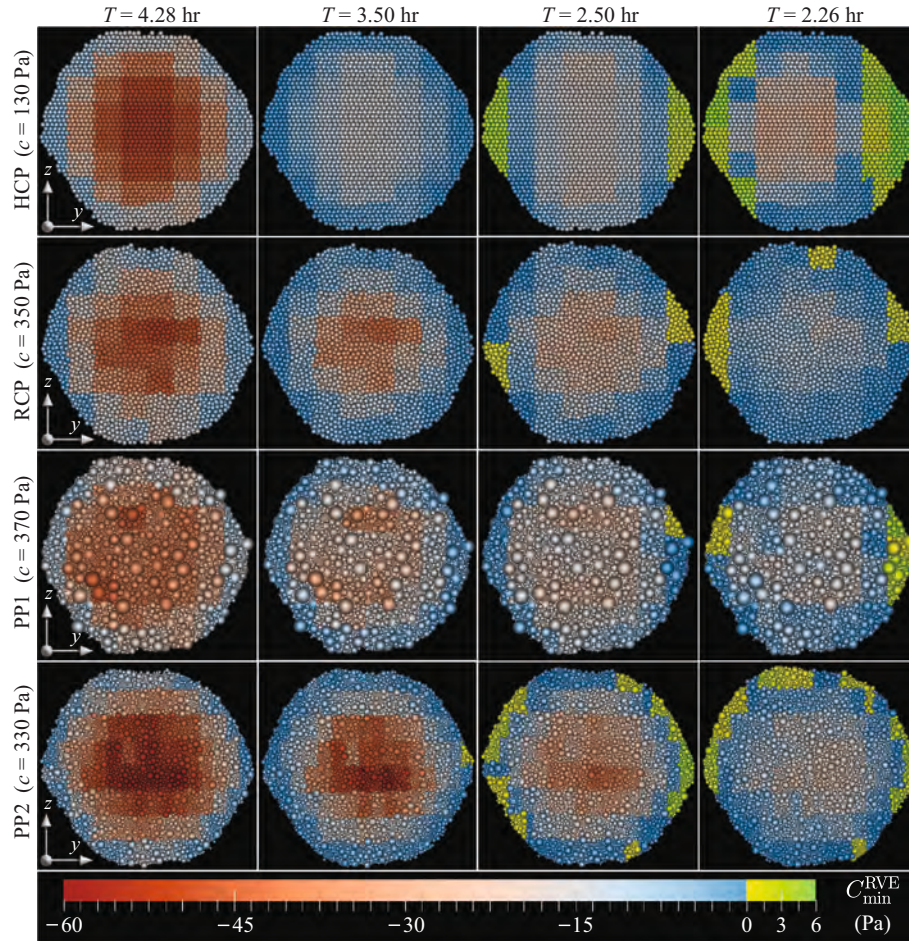
Fig. 3. Distribution of the minimum required cohesion for keeping each RVE stable at different spin periods, C_{min}^{RVE}, over a cross section parallel to the spin axis for the four nominal rubble-pile models with their respective critical interparticle cohesion, $c = c_{crit}$. As the stress analyses are carried out on the scale of RVEs, particles in one RVE share the same color.
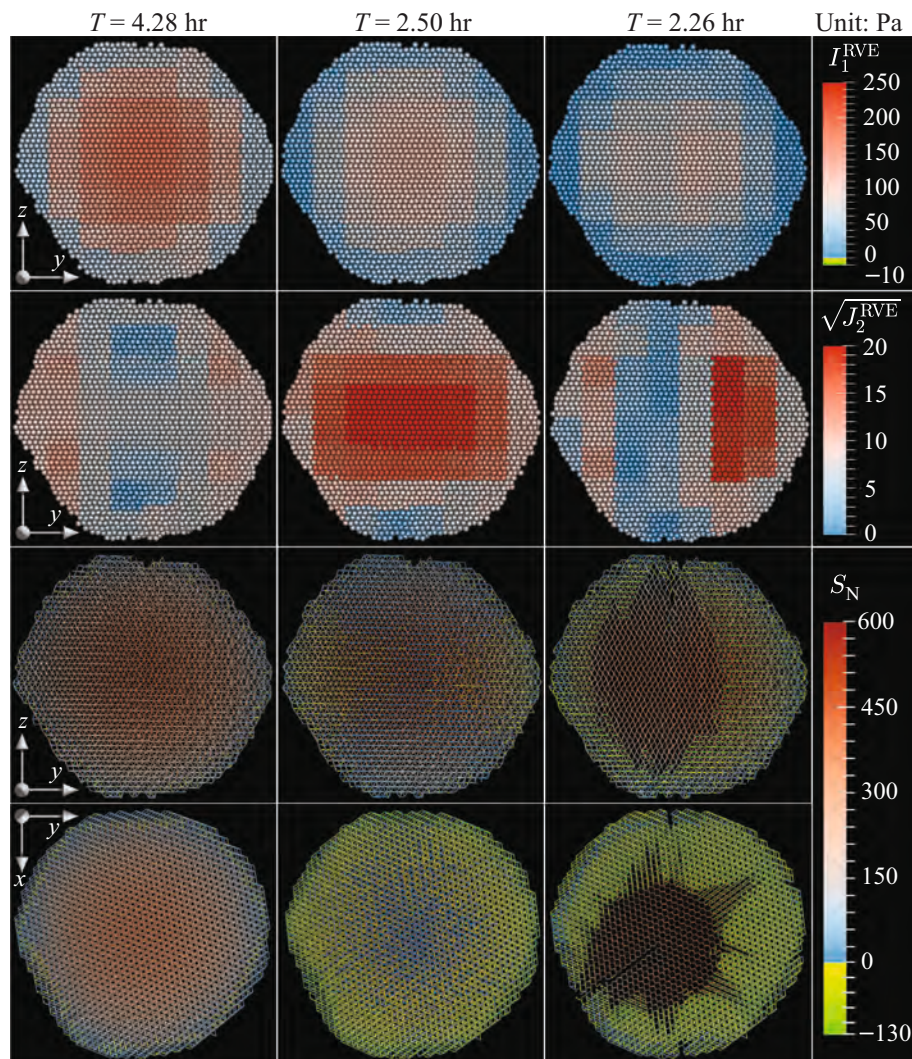
Fig. 4. Distribution of the equivalent pressure, I_1^{RVE} (first row), the equivalent shear stress, $\sqrt{J_2^{\mathrm{RVE}}}$ (second row), and the contact networks (third and bottom rows), over a cross section parallel to the y–z or x–y plane for the HCP model with $c = 130$ Pa at different spin periods. Each column corresponds to a spin state during the spin-up process, as indicated by the spin period given on the top. The third column shows the state of the rubble pile being stable with Didymos' current spin period of 2.26 hr. The orientation of these cross sections is indicated in the corner of each frame in the first column, where z denotes the spin axis. The contact networks in the last two rows are colored by the normal contact strength, S_{N}.

model is notably smaller than other models.

Fig. 5 shows the evolution of the stress-state variables and the contact network of the RCP model. Due to the random particle arrangement, the stress and force chain distribution is not perfectly symmetric about the spin axis. Stress localization could occur in such a structure. The maximum strength of the compressive force chains (~10,000 Pa) is two orders of magnitude larger than that in the HCP model (~600 Pa). Similar to the HCP model, the contact network is dominated by compressive force chains at the slow spin state. With faster spin, the force chains nearly perpendicular to the spin axis change to the tensile direction, while the ones along the spin axis are still in compression. As a result, the center is subject to high shear stress, the poles push inwards toward the center, and the equator is pushed outward, resulting in internal deformation.

As shown in Fig. 2(b), the axis ratio a_3/a_1 of the RCP asteroid gradually decreases during the spin-up process, and the internal porosity slightly increases as particle contacts gradually break. The deformation and the volumetric dilation (changes in a_3/a_1 and η_{inter}) are much more pronounced than those of the HCP model, while the decrease in the coordination number is smaller. This difference in the coordination number is because about one third of the contacts in the HCP model are perpendicular to the spin axis and are easily split up by centrifugal forces. Fig. 6(a) compares the distributions of contact orientations in the RCP model with $c = 350$ Pa at different spin states. The orientations of the force chains are homogeneously distributed in the RCP model at

slow spin, so that the centrifugal force works less efficiently to break the contacts during spin up. Nevertheless, since the centrifugal forces become larger as the spin rate increases, the force chains parallel to the x-y plane gradually break or rearrange themselves in other directions, leading to an asymmetric distribution of contact orientations. By comparing the contact networks in the first and the third columns of Fig. 5, it is apparent that near the center of the rubble pile some force chains parallel to the x-y plane break at the final spin rate producing small cracks in the interior. For c below the critical value, the increasing porosity and cracking cause particle rearrangement in the RCP model, and the body becomes more oblate (see the supplementary video of the RCP model).

3.3.3. Polydisperse packing configuration (PP1)

The PP1 model has a large particle size difference with a size ratio of 8. Since small particles can fill the void between big particles, this model has a higher packing efficiency and a higher friction angle (39°) than the RCP model. The contact number of each particle depends on the size. The largest particle has a maximum contact number of 56, while there are hundreds of small particles having only one contact with others. Therefore, the average contact number N_{cont} of the PP1 model is notably smaller than that of the RCP model and the number of particles with only one contact N_{cont}^1 is much larger. The bulk critical tensile strength $\sigma_{\mathrm{T, crit}}$ and the interparticle critical cohesion c_{crit} of this model are slightly larger than the critical strength values of other models.
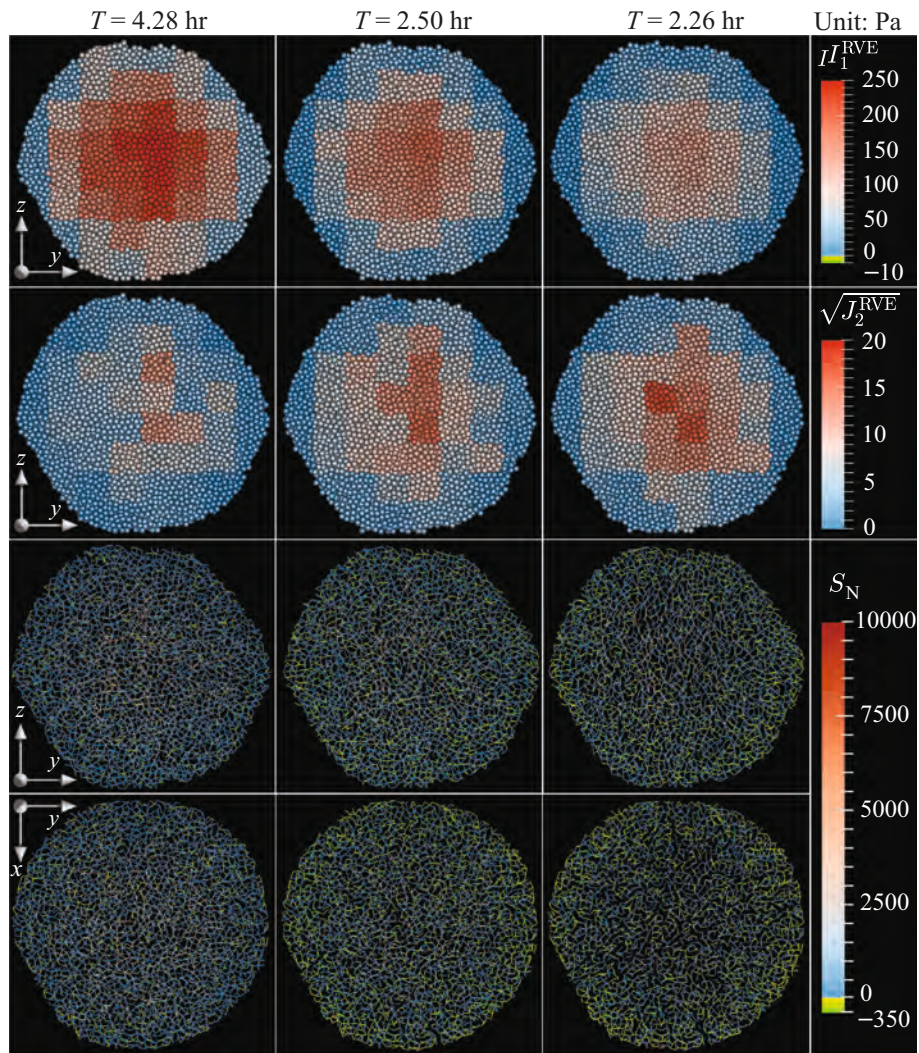
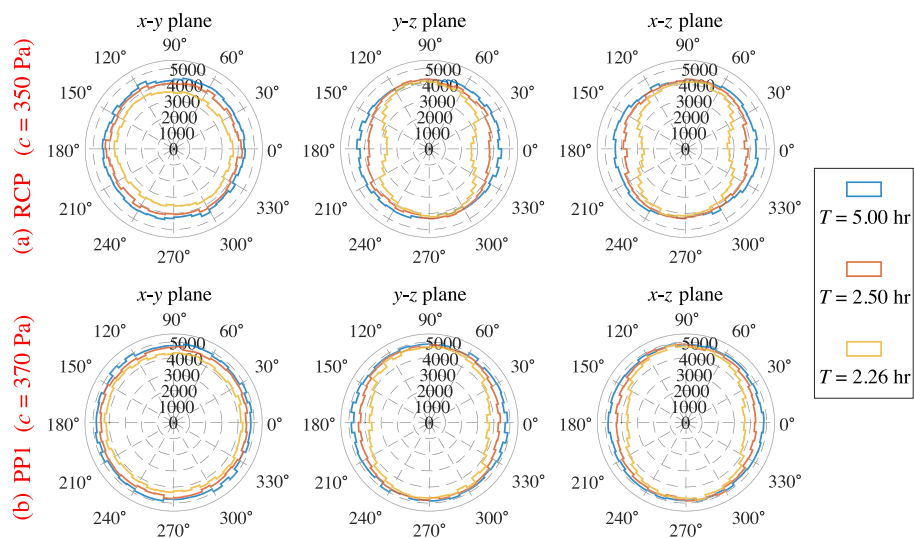**Fig. 5.** Similar to Fig. 4, but for the RCP model with $c = 350$ Pa.

Fig. 6. Contact number and orientation distribution of the RCP (a) and PP1 (b) models with their respective critical interparticle cohesion at different spin periods (denoted by different colors; $\rho_B = 2170$ kg/m^3), where z denotes the spin axis and the x-y plane is parallel to the equatorial plane. The contact number represented in the radial axis is the total number of particle contacts in each angular bin.

Fig. 7 presents the evolution and distribution of the stress-state variables and the contact network of the PP1 model. Similar to the RCP model, the stress localization is also pronounced in this model and the contact network is dominated by compressive force chains at the slow spin state. The orientations of the force chains are homogeneously distributed at slow spin (see Fig. 6(b)). As the spin rate increases, some force chains turn tensile. Compared with the contact network of the RCP model (see Fig. 5), the tensile force chain distribution in the PP1 model is less in favor of the horizontal directions due to the highly heterogeneous particle size distribution. There are some stelliform structures in the force chains indicative of the contact network around big particles. Small particles can reorganize themselves relative to big particles to form some strong irregular agglomerates in the interior. These agglomerates can improve the shear resistance of the rubble-pile interior and reduce the shear stress in the center region. Therefore, contact breakage, deformation, and volumetric dilation behaviors are less pronounced in the PP1 model, as shown in Fig. 2(c) and Fig. 6(b).

As the cohesive force in our SSDEM contact model is size-dependent, the stress distribution in the PP1 model could be much more heterogeneous and asymmetric than in a monodisperse packing for a constant value of c. As shown in the top row of Fig. 7, there is one RVE consisting of relatively smaller particles subject to tensile stress at $T = 2.26$ hr. Since the shear stress in the interior is eased by the dense interior and small particle reorganization, the internal deformation is impeded and the failure of this structure is induced by surface particle movement and

shedding (see the supplementary video of the PP1 model).

3.3.4. Polydisperse packing configuration (PP2) and particle resolution effect

With a particle size ratio of 4, the packing characteristics of the PP2 model are somewhere between the RCP and the PP1 models (see Table 2). Evolution of the rubble-pile properties and distribution of the stress-state variables and the contact network also behave in a manner similar to the two models, as shown in Fig. 2(d) and Fig. 8. The friction angle of 38° is slightly lower than that of the PP1 model. Due to the heterogeneity caused by the particle size distribution, the failure behaviors of this model is surface mass shedding for the Didymos' nominal bulk density, similar to the case of the PP1 model (see the supplementary video of the PP2 model).

We use this packing to explore the effect of particle resolution. As shown in Table 2, the PP3 and PP4 models that are constructed for this purpose have the same particle size distribution and similar packing efficiency as those of the PP2 model. The interparticle critical cohesion estimated for these two models are almost the same as that of the PP2 model. As the coordination number of the low-resolution model at the end of the spin-up processes is larger (see Table 2), the macroscopic maximum critical cohesion $C_{max, crit}$ slightly increases with a lower particle resolution (see Table 3). This could be explained by that, in a lower-resolution model, the geometric interlocking of the cohesive constituent particles is more effective, so that it is harder to break
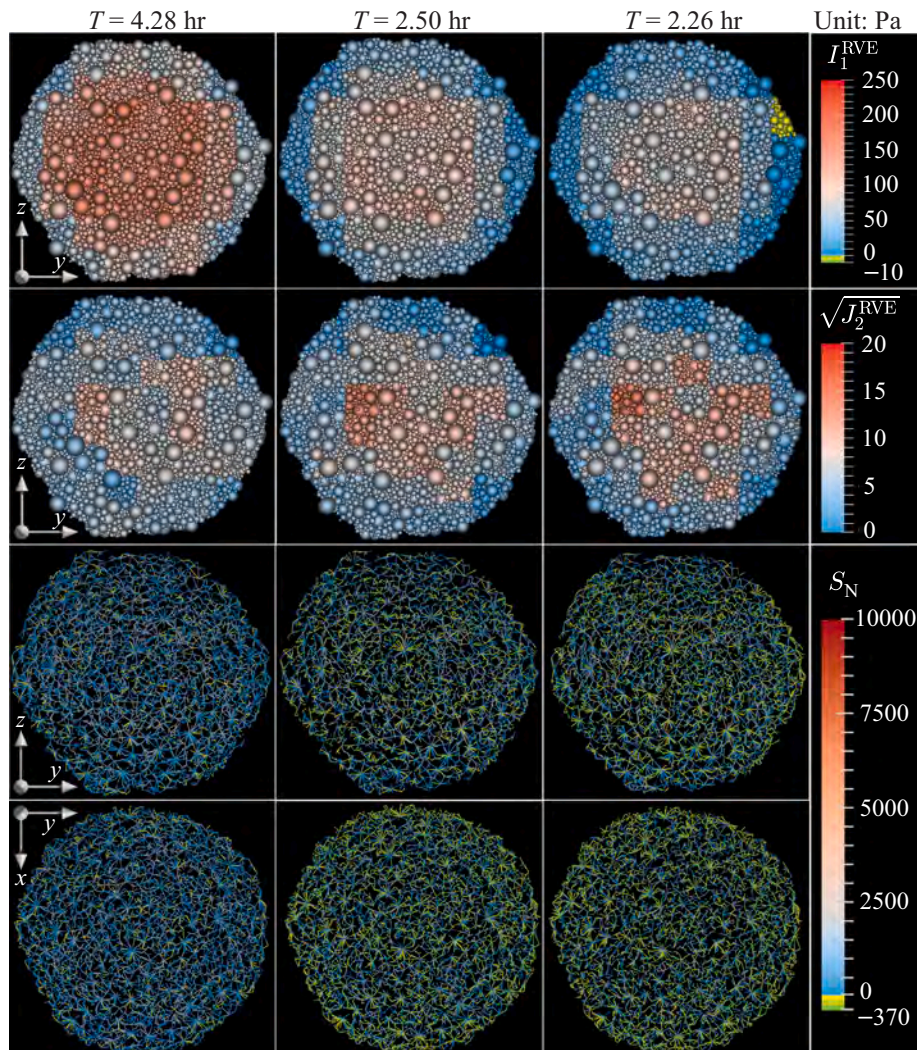

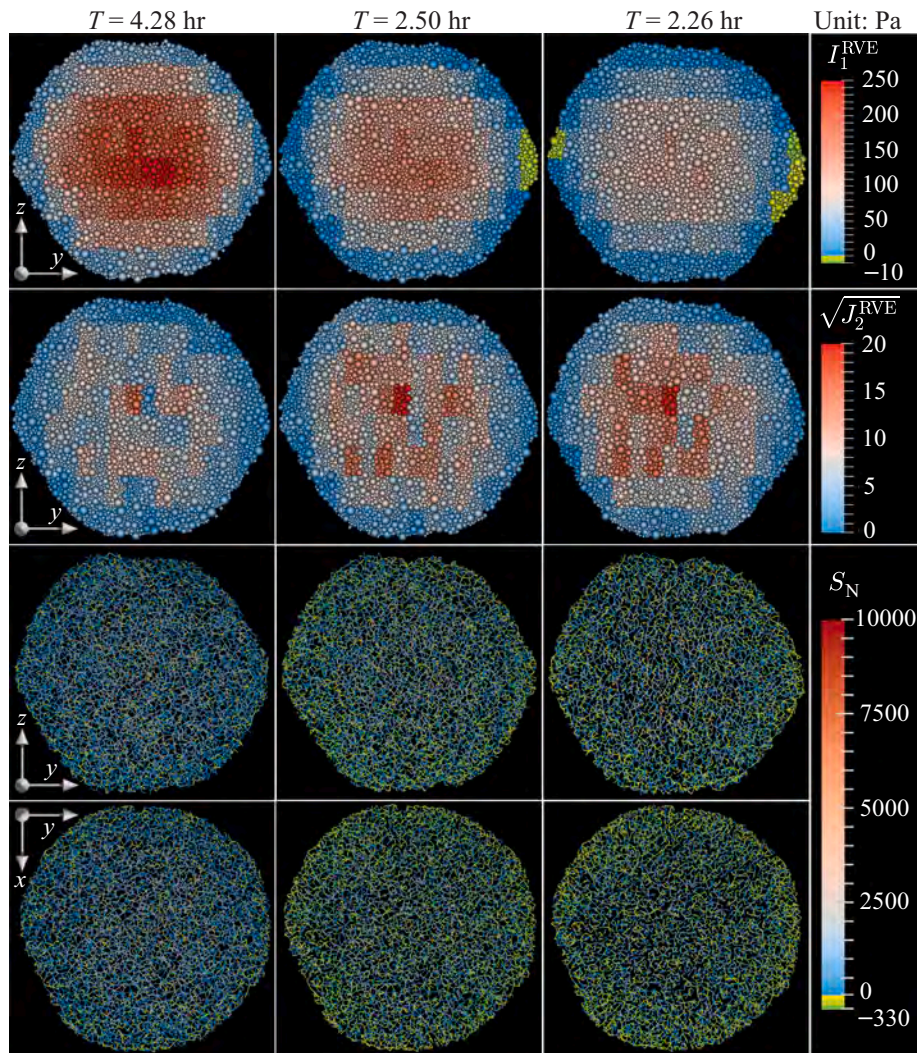**Fig. 7.** Similar to Fig. 4, but for the PP1 model with $c = 370$ Pa.

Fig. 8. Similar to Fig. 4, but for the PP2 model with $c = 330$ Pa.

particle contacts.

However, the macroscopic minimum critical cohesion $C_{min, crit}$ estimated for the PP3 and PP4 models is notably smaller than that of the PP2 model (especially for the case of PP4 model, where $C_{min, crit}$ is negative, meaning no cohesion is needed; see Table 3). As we discussed in Section 2.3.3, the stress analyses could be affected by the chosen size of the RVEs. In the PP4 model ($N = 1562$), where the size of the RVEs (containing ∼300 particles in this study) is comparable to its own radius, the averaging formalism used in the stress analyses largely underestimates the shear stress in local regions. Choosing a smaller RVEs for the stress analyses could provide a better estimate but may not be reliable for the reason discussed in the end of Section 2.3.3. Therefore, in order to make valid estimates on $C_{min, crit}$ and properly reveal the local stress distribution, the particle resolution should be high enough (at least the resolution of the PP3 model).

3.4. Influence of the bulk density

Current observations can only constrain the bulk density of Didymos within the range of [1820, 2520] kg/m³. Paper I has shown that some Didymos rubble-pile models (i.e., the HCP model and the PP1 model with a higher density core) can be stable with bulk densities close to the upper limit. Here we use the procedure described in Section 3.3 to estimate c_{crit}, $\sigma_{T, crit}$, $C_{max, crit}$, and $C_{min, crit}$ for the HCP, RCP, PP1, and PP2 models within this bulk density range. Given that the system mass is

relatively well constrained with Kepler's third law and the uncertainty in the bulk density mainly comes from the volume estimate error, we scale the bulk radius and particle size of our rubble-pile models to achieve the desired bulk density.

Our simulation results show that not only the minimum required cohesion significantly varies with the bulk density, but also the failure behaviors strongly depend on the bulk density. The four supplementary videos present the spin-up process of each Didymos rubble-pile model with $c = c_{crit} - 10$ Pa for three representative bulk densities (a set of stereo movies for the PP1 models are also available online). It is evidenced that, with low bulk densities, the Didymos rubble piles tend to fail by tensile disruption,[7] and with high bulk densities, they tend to fail by shedding surface material. When the bulk densities are close to the nominal value (i.e., 2170 kg/m³), the rubble piles show pronounced internal deformation.

Table 4 summarizes the values of c_{crit} of these four models with

---

[7] In this case, the rubble pile first breaks apart into several fragments, and the rotation, mutual gravity, internal collapse, and collisions of these fragments cause some particles shedding from their surfaces. Some of these particles then continuously fall back on the surface of the major remnant under its gravity in later stages. As the coefficients of restitution are nonzero, these particles' bouncing behaviors can last for a relatively long time (Jiang et al., 2016; Thuillet et al., 2018).

different bulk densities. Except for the HCP model with $\rho_B \gtrsim 2450$ kg/m^3, all the models require the material to be cohesive to keep their shape stable, consistent with the findings of paper I. The coordination number and the internal packing efficiency at the stable end state where the rubble pile's spin period $T = 2.26$ hr are also given in this table. It is noted that, with a larger bulk density, a rubble-pile model needs a smaller c_{crit} to maintain its stability, and $N_{cont, end}$ tends to decrease while $\eta_{inter, end}$ is almost unchanged.

Fig. 9 shows how c_{crit}, $N_{cont, end}$, and the macroscopic critical tensile strength $\sigma_{T, crit}$ change with the bulk density for the four models. There are significant differences in the values of c_{crit} and its dependence on ρ_B between different models. The variation in the coordination number of the HCP, RCP and PP2 models is much more prominent than that of the PP1 model. As a result, the value of $\sigma_{T, crit}$ (calculated by Eq. (4)) shows different dependencies on ρ_B for the four models.

It is interesting to note that all the four models have nearly identical critical tensile strengths for the bulk density of ~2150 kg/m^3. This density is close to the bulk density for which the centrifugal force equals the gravitational force, i.e., when the spin rate of the rubble pile $\omega = \sqrt{4\pi G \rho_B/3}$. Hereafter, we call this bulk density the "transition bulk density", $\rho_{B, tran}$. Compared to the critical tensile strength of the RCP model, both the PP1 and PP2 models have a lower $\sigma_{T, crit}$ when their bulk densities are below this density threshold, while they have a higher $\sigma_{T, crit}$ when $\rho_B > \rho_{B, tran}$. For example, when $\rho_B = 1820$ kg/m^3, $\sigma_{T, crit} = 52$ Pa for the RCP model and 38 Pa for the PP1 model; however, when $\rho_B = 2520$ kg/m^3, $\sigma_{T, crit} = 7$ Pa for the RCP model and 12 Pa for the PP1 model.

To explain the relation of $\sigma_{T, crit}$ and ρ_B with different models, one should first noted that for $\rho_B < \rho_{B, tran}$, the centrifugal force triumphs over the gravitational force, so that the rubble pile is in a strength-dominated regime and its failure region is in tension state; while for $\rho_B > \rho_{B, tran}$, the rubble pile is in a gravity-dominated regime and the failure region is usually in compression state and destabilized by shear failure. Due to the differences in particle size distribution and arrangement, our rubble-pile models could have different responses to the spin-up acceleration in the strength-dominated and gravity-dominated regimes, and require different levels of c_{crit} and $\sigma_{T, crit}$ (see the supplementary videos of the four models).

In the HCP model, when $\rho_B > \rho_{B, tran}$, the high shear resistance due to the cannonball packing can impede the structural shear failure during spin up, and only a small amount of cohesion is needed; when ρ_B becomes slightly smaller than $\rho_{B, tran}$, the tensile stress need to be balanced by intensive cohesion, and thus, the minimum required c_{crit} dramatically increases; with further decreases in ρ_B, small increments in c_{crit} are sufficient to keep the structure intact. As shown in Fig. 9(b), contact breakages during spin up are forbidden in a stable HCP model with $\rho_B < \rho_{B, tran}$ for preventing tensile failure.

In the RCP model, strong interparticle tensile strength is also required to prevent contact breakages when $\rho_B < \rho_{B, tran}$. Fig. 10(a) compares the force chain distribution at $T = 2.26$ hr with the initial state
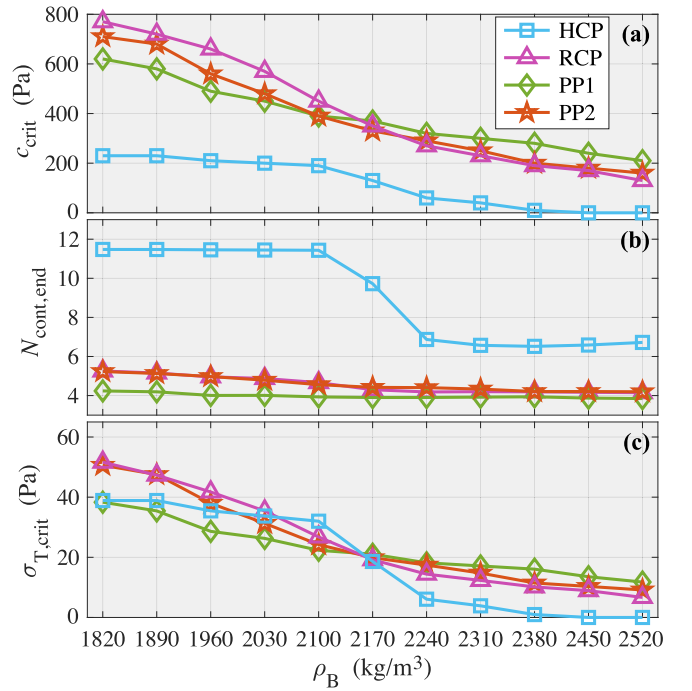

Fig. 9. Interparticle critical cohesion (a), coordination number at $T = 2.26$ hr (b), and macroscopic tensile strength (c) against bulk density for the four Didymos rubble-pile models within the possible range of Didymos's bulk density.

where $T = 5.00$ hr for the case of $\rho_B = 1820$ kg/m^3. It is evidenced that little contact is lost in this case. Furthermore, most of the force chains parallel to the x-y plane are in tension and the number of tensile force chains are nearly equal in number to compressive force chains. Therefore, the RCP model is mainly maintained by its tensile strength in the case of $\rho_B = 1820$ kg/m^3 but would fail in tension with a smaller c_{crit}. When entering the shear failure region, i.e., $\rho_B > \rho_{B, tran}$, as shown in Fig. 11(a), extensive contact breakages are allowed without inducing failure, and only a small amount of tensile force chains is sufficient to maintain the structural stability.

Compared with the RCP model with $\rho_B = 1820$ kg/m^3 for the critical stability case, more particle contacts break in the PP1 model during spin up and the ratio of tensile-to-compressive force chains is smaller (see Fig. 10(b)). Due to the heterogeneous particle size distribution, the big particles in the PP1 model provide larger contact areas for small particles (and thus greater cohesive forces) to form strong particle agglomerates. The improved interlocking between these irregular agglomerates supplies additional tensile and shear resistance. As a consequence, in the strength-dominated regime where $\rho_B < \rho_{B, tran}$ and tensile failure occurs, the PP1 model can be stable with a smaller c. Although the interior can

Table 4

Interparticle critical cohesion and rubble-pile properties at the end state of the Didymos rubble-pile models with different bulk densities.

ρ_B	HCP			RCP			PP1			PP2		
(kg/m^3)	c_{crit} (Pa)	$N_{cont, end}$	$\eta_{inter, end}$	c_{crit} (Pa)	$N_{cont, end}$	$\eta_{inter, end}$	c_{crit} (Pa)	$N_{cont, end}$	$\eta_{inter, end}$	c_{crit} (Pa)	$N_{cont, end}$	$\eta_{inter, end}$
1820	230	11.475	0.741	770	5.257	0.641	620	4.238	0.733	710	5.230	0.685
1890	230	11.473	0.741	720	5.154	0.641	580	4.192	0.732	680	5.130	0.685
1960	210	11.457	0.741	660	4.958	0.641	490	4.008	0.732	560	4.975	0.685
2030	200	11.446	0.741	570	4.874	0.641	440	4.010	0.732	480	4.786	0.685
2100	190	11.434	0.741	450	4.664	0.641	390	3.932	0.732	390	4.559	0.685
2170	130	9.725	0.740	350	4.299	0.641	370	3.901	0.732	330	4.421	0.685
2240	60	6.870	0.740	270	4.186	0.641	320	3.902	0.732	290	4.407	0.685
2310	40	6.570	0.740	230	4.200	0.641	300	3.922	0.732	250	4.333	0.685
2380	10	6.518	0.740	190	4.192	0.641	280	3.938	0.732	200	4.207	0.685
2450	0	6.586	0.740	170	4.114	0.641	240	3.872	0.732	180	4.207	0.685
2520	0	6.719	0.741	130	4.021	0.641	210	3.848	0.732	160	4.200	0.685
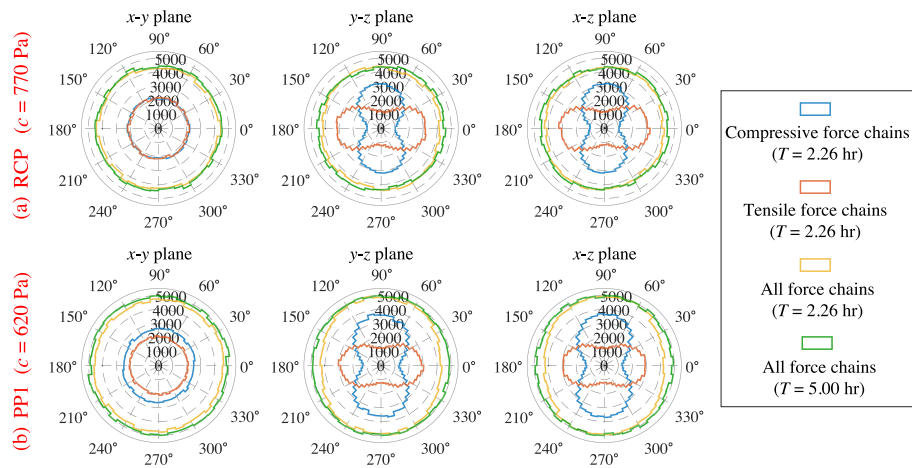
Fig. 10. Orientation distribution of compressive/tensile contact force chains of the RCP (a) and PP1 (b) models with their respective critical interparticle cohesion at different spin periods ($\rho_B = 1820$ kg/m^3), where z denotes the spin axis and the x-y plane is parallel to the equatorial plane. The spin period and force chain property for each curve are indicated in the legend.

stay stable thanks to the presence of strong agglomerates, in the gravity-dominated regime, where $\rho_B > \rho_{B, \text{tran}}$ and shear failure occurs, the heterogeneous distribution of strength at the surface requires a larger c than that of the monodisperse case to keep all the surface particles stable. As shown in Fig. 11(b), a relatively large number of tensile force chains is required to stabilize the PP1 model when $\rho_B = 2520$ kg/m^3. The values of c_{crit} and $\sigma_{T, \text{crit}}$ of the PP2 model can be explained in a similar way.

Our investigation not only provides quantitative estimates for the strength of Didymos within the possible bulk density range, but also reveals the different failure behaviors associated with the bulk density and particle size distribution. This provides important implications for addressing the formation of this binary system (see Section 4.2 below).

4. Discussion

4.1. Required amount of cohesion: continuum versus discrete approach

The presented analysis is based on SSDEM simulations. However, the common-used analytical approach (Holsapple, 2007) provides a more efficient way to evaluate the minimum required cohesion of a rubble pile based on the continuum theory. We, therefore, compare our SSDEM results with those derived by such a continuum approach. By definition, the SSDEM explicitly models the component particles as discrete elements. The continuum approach treats the components as a continuum

medium, which could be appropriate for analyzing some macroscopic behaviors. However, due to lack of reliable constitutive laws, this treatment is not appropriate when the dynamical processes is affected by particle geometry and interlocking (Sheng et al., 2004).

Following the method introduced in Holsapple (2007), we compute the stress-state variables of Didymos' DEEVE at the spin period of 2.26 hr (see Section 3.1 for the definition of the DEEVE) and evaluate the required cohesion based on the Drucker-Prager failure criterion (i.e., Eq. (2)). Note that the continuum approach relies on global volume-averaged stresses and assumes that the structure fails globally. As noted in Holsapple (2007) and Hirabayashi (2015), and as found in our SSDEM simulations, the failure of a rubble pile is initiated locally rather than globally. Therefore, the actual failure occurs at a lower spin than that found by the continuum approach. That is, for a given spin, this approach gives the lower bound of the required bulk cohesion of a rubble pile.

Fig. 12 compares the critical cohesive strength derived by our SSDEM approach and the continuum theory. The critical bulk cohesion $C_{\text{max, crit}}$ can serve as a suitable parameter for these comparisons as the continuum theory also measures the bulk cohesion. Except for the case of the HCP model, $C_{\text{max, crit}}$ of the RCP and PP1/2 models at high densities is close to the estimate of the continuum theory. The crystallized structure of the HCP model strengthens the influence of particle interlocking, and therefore, its behavior and spin limit are hard to be predicted by the continuum theory. The random arrangement of the other three models
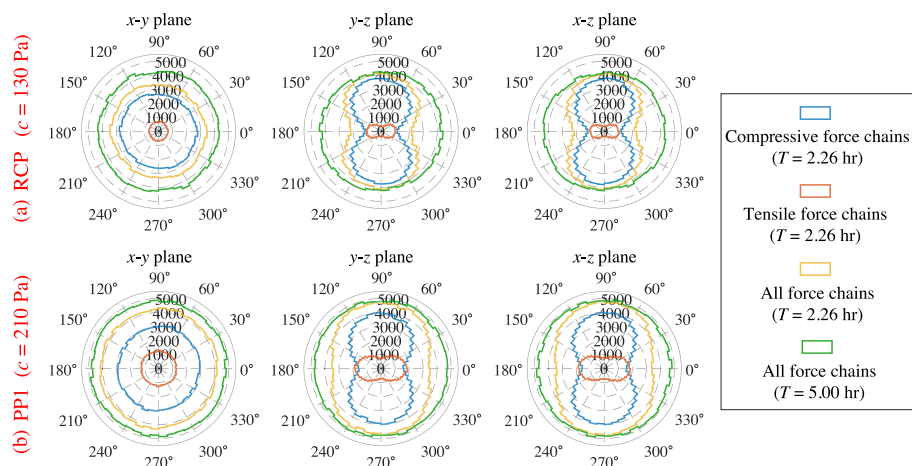
Fig. 11. Similar to Fig. 10, but for the case of $\rho_B = 2520$ kg/m^3.
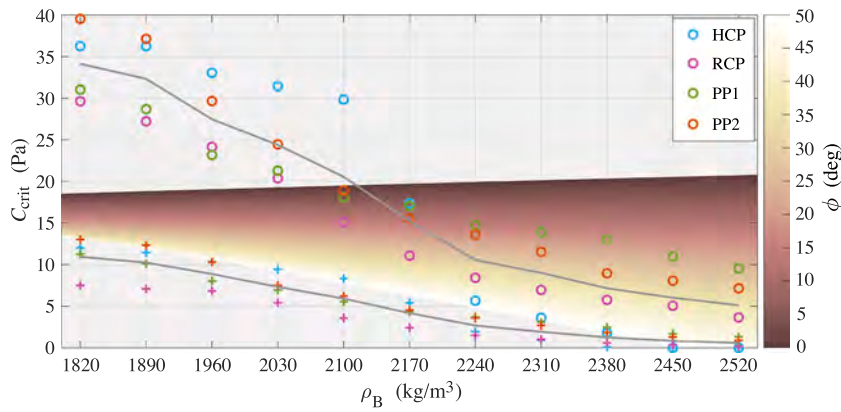
Fig. 12. Macroscopic critical cohesive strength against bulk density for the four Didymos rubble-pile models within the possible range of Didymos's bulk density. The circles denote the values of $C_{\mathrm{max,\,crit}}$ and the plus signs denote the values of $C_{\mathrm{min,\,crit}}$. The results for different packings are indicated by the colors, as indicated in the legend. The gray curves show the mean values of $C_{\mathrm{max,\,crit}}$ and $C_{\mathrm{min,\,crit}}$ averaged over the four packings. For comparison, the critical cohesion derived by the continuum theory is presented in the whitish to reddish background, where the color represents the corresponding friction angle for each estimate (ranging from 0° to 50°, as indicated in the colorbar).

makes their behavior a better match to the continuum theory.

Nonetheless, the critical bulk cohesion value derived by these two approaches show opposite dependencies on the friction angle. Within the explored bulk density range, the continuum theory predicts that Didymos needs larger cohesion to maintain its stability for a smaller friction angle. In turn, our simulation results show that $C_{\mathrm{max,\,crit}}$ is decreasing with a smaller friction angle (recall that, 39° for PP1; 38° for PP2; 30° for RCP). The differences indicate that the spin limit of a cohesive rubble pile is sensitive to the particle size distribution and arrangement, which cannot be well captured in a continuum method. Therefore, carrying out SSDEM simulations is important for making accurate estimates for the material properties and evolution of cohesive rubble-pile small bodies. Dedicated exploration into this subject will be addressed in our future work.

It is also interesting to note that, the critical bulk cohesion derived by the SSDEM simulations is close to the values derived by the continuum theory for a bulk density larger than $\rho_{\mathrm{B,\,tran}}$, but for the lower bulk densities, the continuum theory gives a cohesion value much smaller than our estimates. This inconsistency may come from the differences in the failure modes observed in the SSDEM models for low and high densities as the dynamical regime transmits from strength-dominated ones to gravity-dominated ones.

Fig. 13 shows the distribution of stress-state variables of the four Didymos rubble-pile models with their respective critical cohesion at the spin period of 2.26 hr. It is clear to see that the HCP model behaves very differently than the other three models. The hollow triangles denote the results obtained by the continuum approach, showing that the stress state is always in compression for all the bulk densities considered in this study. For the SSDEM models, the stress state depends on the bulk density of the rubble pile. For low densities ($<\rho_{\mathrm{B,\,tran}}$), the stress state close to failure (i.e., the stress state that corresponds to the largest C) is in tension. With an increasing bulk density, the stress state at the failure region goes from tensile to pure shearing, and then to compression.

Our study reveals that failure stress states in a discrete rubble pile are different from those derived by the continuum theory-based approach using a global volume-averaged stress evaluation. It is recognized that, for a strength-dominated rubble pile, the results of the average method are only approximate (Holsapple, 2007). Therefore, this continuum-theory approach must be used with caution to estimate the cohesive strength of a rubble pile, especially in the strength regime.

Based on similar continuum medium assumptions and the Drucker-Prager failure criterion, Naidu et al. (2020) estimated the critical cohesion of Didymos to be ~20 Pa using the Finite Element Method (FEM) assuming $\rho_{\mathrm{B}} = 2170$ kg/m³. Since this approach gives the upper bound of the required bulk cohesion of a rubble pile (see Hirabayashi et al., 2020, for details about this approach), this estimate is consistent with our results. However, the region most sensitive to failure at the current spin period in their FEM model is located at the center of Didymos, which is opposite to our finding that the surface is more likely

to fail first (as shown in Fig. 3). This inconsistency has been revealed and discussed in Zhang et al. (2018). The cause for this difference arises from the fact that the FEM and other types of continuum models do not capture a surface region with lower cohesion as is expected for a rubble-pile model. Instead, these models assume a constant macroscopic cohesive strength all over the body. The cohesion distribution of an asteroid is still poorly know but very likely to be heterogeneous (as indicated by some surface features on asteroid Bennu, e.g., Barnouin et al., 2019; Daly et al., 2020). The data returned by the DART and Hera missions may allow determining the cohesion distribution of Didymos based on a combination of our SSDEM modeling and the FEM modeling.

4.2. Possible physical properties of Didymos

With the nominal value of the bulk density derived from current observations, Fig. 9 shows that the bulk critical tensile strength $\sigma_{\mathrm{T,\,crit}}$ of Didymos has the same value for all considered packings. Therefore, provided that the actual density is close to the nominal value, we can predict that $\sigma_{\mathrm{T,\,crit}}$ of Didymos is about 20 Pa, the bulk cohesion $C_{\mathrm{max,\,crit}}$ is about 15 Pa and the surface cohesion $C_{\mathrm{min,\,crit}}$ is about 5 Pa for a friction angle of 38°. If the actual density is lower, $\sigma_{\mathrm{T,\,crit}}$ (and C_{crit}) will be higher, and vice versa. However, in such cases, the quantitative predictions on $\sigma_{\mathrm{T,\,crit}}$ could be inaccurate, unless we have detailed information on the actual particle size distribution of Didymos.

Our simulation results show a clear dependency of the failure mode on the bulk density. For densities lower than the nominal value, our Didymos models tend to fail in tension, while at higher densities, they experience shear failure, which leads to internal deformation or surface mass shedding. Therefore, if surface mass shedding is at the origin of this binary system (i.e., the formation processes proposed by Walsh et al., 2008), the bulk density of Didymos is very likely to be equal to or higher than the nominal value, and Dimorphos is also likely to be a rubble pile via reaccumulation of the shedding material.

Note that this study ignores the potential gravitational influence of Dimorphos on the stability of Didymos, which will be analyzed in the next paper of this series. Moreover, it may be possible that Didymos is still in a reshaping mode currently, with continuous mass shedding if it is spun up. In this case, the current radar-derived shape is not in the stable state and the actual physical properties may be different from those indicated by our stability analysis.

4.3. Implication for measurements of Didymos by space missions

The DART mission (NASA) will perform the impact on Dimorphos in late 2022, and release an onboard cubesat LICIACube (Light Italian Cubesat for Imaging of Asteroids) ten days before the impact to monitor the cratering process and the evolution of the resulting ejecta. The camera resolution of LICIACube is on the order of one meter, which may be able to characterize the system stability and some local surface
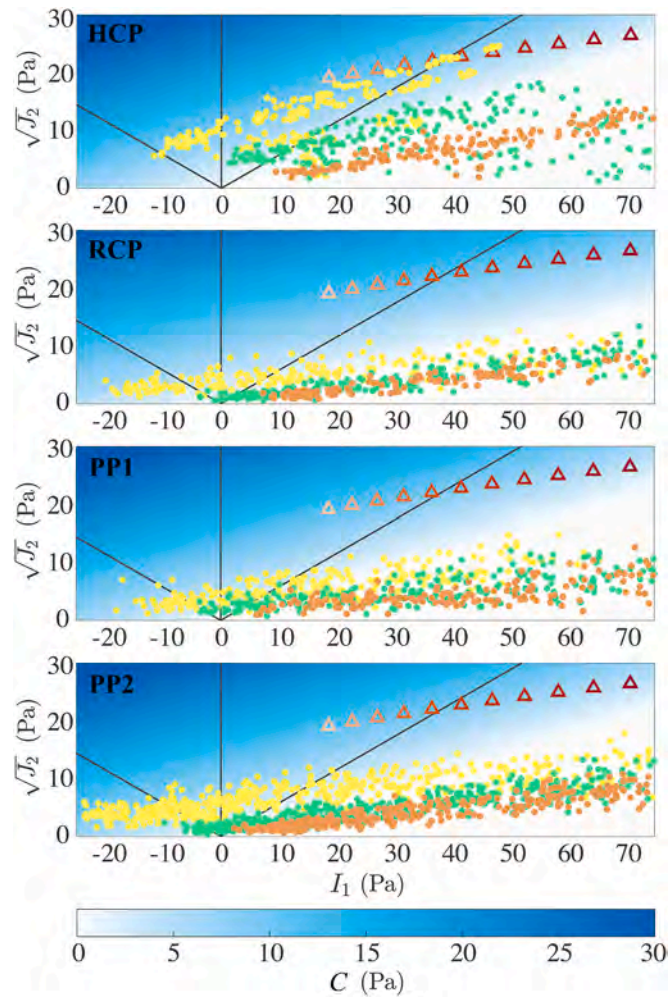
Fig. 13. Distribution of the stress-state variables of RVEs in the $I_1-\sqrt{J_2}$ plane of the four rubble-pile models at their respective critical state. The results of different densities are shown in different colors, where yellow solid circles correspond to the case of $\rho_B = 1820$ kg/m^3, green solid circles correspond to $\rho_B = 2170$ kg/m^3, and orange solid circles correspond to $\rho_B = 2520$ kg/m^3. The three black lines indicate the failure mode in uniaxial tension ($\sqrt{J_2} = -I_1/\sqrt{3}$), pure shear ($I_1 = 0$ Pa), uniaxial compression ($\sqrt{J_2} = I_1/\sqrt{3}$). The triangles present the stress-state variables at failure obtained by the continuum theory for different bulk densities (ρ_B increases from the left to the right within the range of [1820, 2520] kg/m^3 with an interval of 700 kg/m^3). The blue background color indicates the minimum required cohesive strength derived by the Drucker-Prager failure criterion (Eq. (2)). (For interpretation of the references to color in this figure legend, the reader is referred to the web version of this article.)

features before and after the impact (Cheng et al., 2020). The expected returned data may also reveal the boulder size and density distribution on Didymos and Dimorphos (Pajola et al., 2020). This information will help us to constrain the cohesion of Didymos and make connections with boulder sizes within the framework of this study.

Our study shows that the structural stability and evolution of Didymos is very sensitive to its material cohesive strength and particle size distribution. With the estimated critical cohesion at the nominal bulk density case, we find that a small decrease of 0.0001 hr in the spin period would destabilize the Didymos' structure. If Didymos has the minimum required cohesion to maintain its shape at the current spin period, spin period variations caused by orbital period changes of Dimorphos due to the DART impact may result in reshaping or mass shedding. Combined with the pre- and post-impact Didymos-Dimorphos system evolution analyses (e.g., Yu et al., 2018; Hirabayashi et al., 2019; Agrusa et al.,

2020), the measurements carried out by the space missions will help us to refine our estimates on the material strength and interpret the internal structure and evolutionary history of this binary system. Future work will focus on full two-rigid/rubble-pile-body simulations to investigate the long-term dynamical evolution of this system after the DART impact (e.g., Agrusa et al., in preparation).

On the other hand, if Didymos is cohesive enough to keep its global stability before and after the impact, local surface motion or cratering could still be triggered by the impact of DART's ejecta. Evidence of recent surface movements, craters, or even landslides could then be looked for by Hera.

The Hera mission (ESA) will perform a rendezvous with Didymos in early 2027. Although the main objective is the full characterization of the impact outcome on Dimorphos, including measurements of its mass, structure, and composition, as well as investigation of the crater, Didymos will also be carefully imaged (Michel et al., 2020). The combination of observed surface and global characteristics and our modeling can allow inferring its actual material properties. The DART crater and possible secondary craters on Didymos and Dimorphos could help us to refine our cohesion estimate and distinguish the strength versus gravity cratering regime of their surfaces.

Furthermore, our analyses on the correlation of critical cohesion, bulk densities, and failure behaviors will contribute to the understanding of the formation scenarios of this binary system based on Hera's measurements. For example, if strong evidence of mass shedding correlated with a confirmation that the density is equal to or higher than the nominal value is found by Hera, Dimorphos is very likely to be formed through the YORP-induced mass shedding as described in Walsh et al. (2008). In that case, images and radar sounding of Dimorphos should also point to a rubble-pile structure for this 150-m-sized object. On the other hand, if the measurements show evidence of lower densities while other evidences still in favor of this formation mechanism (e. g., rubble-pile Dimorphos, similar composition in Didymos and Dimorphos), it would mean that cohesion is not homogeneously distributed in the progenitor of this system and a weak surface is required to induce mass shedding in the past (such as the failure process shown in Hirabayashi, 2015; Sánchez and Scheeres, 2018).

5. Conclusions and perspectives

Using the soft-sphere discrete element model including cohesion, we study the failure conditions and behaviors of several Didymos rubble-pile representatives under the YORP spin-up process. A novel approach is introduced that allows us to quantify the critical cohesion of these rubble-pile models.

We find that Didymos must have a cohesion around 15 Pa in general (the exact amount depends on its particle arrangement and size distribution) to maintain its shape at the nominal density of 2170 kg/m^3. With this critical cohesion level, Didymos is at the edge of maintaining a stable shape. A rapid small decrease in the spin period on the order of 0.0001 hr would excite the rubble-pile structure and lead to some reshaping or mass shedding. Whether the DART impact could partially or globally destabilize this system would require further investigation into the full two-body gravitational dynamics and the ejecta evolution.

Our analyses on the correlation between critical cohesion and bulk densities reveal that the lower-density Didymos in the strength-dominated regime would be disrupted by tensile failure and the higher-density Didymos in the gravity-dominated regime would fail through surface shedding and internal deformation during YORP spin-up process.

These findings have important implications on what the DART and Hera missions may observe when they arrive at the Didymos-Dimorphos system. Comparison of actual measurements with this study will allow constraining the history and mechanical properties of this system. For instance, we predict that surface mass shedding may account for the formation of this system if Hera could find evidence of mass shedding

and confirm that the actual bulk density of Didymos is close to or larger than the estimated nominal value and Dimorphos has a rubble-pile structure with similar composition.

In addition, Hera may also find unexpected physical features and our modeling can be further extended to determine the source of these features. New data combined with modeling will thus allow major advances in our understanding of this kind of binary systems with a fast-spinning top shape primary.

Note that this study only considered Didymos as a single asteroid. Future studies will consider the potential influence of the presence of Dimorphos on the behavior of Didymos and investigate the full-two-rubble-pile-body dynamics.

Supplementary data to this article can be found online at https://doi.org/10.1016/j.icarus.2021.114433.

Declaration of Competing Interest

None.

Acknowledgements

References

Agrusa, H.F., Richardson, D.C., Davis, A.B., Fahnestock, E., Hirabayashi, M., Chabot, N. L., Cheng, A.F., Rivkin, A.S., Michel, P., 2020. A benchmarking and sensitivity study of the full two-body gravitational dynamics of the DART mission target, binary asteroid 65803 Didymos. Icarus 349, 113849. https://doi.org/10.1016/j.icarus.2020.113849.

Arakawa, M., Saiki, T., Wada, K., Ogawa, K., Kadono, T., Shirai, K., Sawada, H., Ishibashi, K., Honda, R., Sakatani, N., Iijima, Y., Okamoto, C., Yano, H., Takagi, Y., Hayakawa, M., Michel, P., Jutzi, M., Shimaki, Y., Kimura, S., Mimasu, Y., Toda, T., Imamura, H., Nakazawa, S., Hayakawa, H., Sugita, S., Morota, T., Kameda, S., Tatsumi, E., Cho, Y., Yoshioka, K., Yokota, Y., Matsuoka, M., Yamada, M., Kouyama, T., Honda, C., Tsuda, Y., Watanabe, S., Yoshikawa, M., Tanaka, S., Terui, F., Kikuchi, S., Yamaguchi, T., Ogawa, N., Ono, G., Yoshikawa, K., Takahashi, T., Takei, Y., Fujii, A., Takeuchi, H., Yamamoto, Y., Okada, T., Hirose, C., Hosoda, S., Mori, O., Shimada, T., Soldini, S., Tsukizaki, R., Iwata, T., Ozaki, M., Abe, M., Namiki, N., Kitazato, K., Tachibana, S., Ikeda, H., Hirata, N., Hirata, N., Noguchi, R., Miura, A., 2020. An artificial impact on the asteroid (162173) ryugu formed a crater in the gravity-dominated regime. Science 368, 67–71. https://doi.org/10.1126/science.aaz1701.

Barnouin, O.S., Daly, M.G., Palmer, E.E., Gaskell, R.W., Weirich, J.R., Johnson, C.L., Al Asad, M.M., Roberts, J.H., Perry, M.E., Susorney, H.C.M., Daly, R.T., Bierhaus, E.B., Seabrook, J.A., Espiritu, R.C., Nair, A.H., Nguyen, L., Neumann, G.A., Ernst, C.M., Boynton, W.V., Nolan, M.C., Adam, C.D., Moreau, M.C., Rizk, B., Drouet D'Aubigny, C.Y., Jawin, E.R., Walsh, K.J., Michel, P., Schwartz, S.R., Ballouz, R.L., Mazarico, E.M., Scheeres, D.J., McMahon, J.W., Bottke, W.F., Sugita, S., Hirata, N., Hirata, N., Watanabe, S.I., Burke, K.N., Dellagiustina, D.N., Bennett, C.A., Lauretta, D.S., Team, Osiris-Rex, 2019. Shape of (101955) Bennu indicative of a rubble pile with internal stiffness. Nat. Geosci. 12, 247–252. https://doi.org/10.1038/s41561-019-0330-x.

Chau, K., Wong, R., Wu, J., 2002. Coefficient of restitution and rotational motions of rockfall impacts. Int. J. Rock Mech. Min. Sci. 39, 69–77. https://doi.org/10.1016/S1365-1609(02)00016-3.

Cheng, A.F., Rivkin, A.S., Michel, P., Atchison, J., Barnouin, O., Benner, L., Chabot, N.L., Ernst, C., Fahnestock, E.G., Kueppers, M., Pravec, P., Rainey, E., Richardson, D.C., Stickle, A.M., Thomas, C., 2018. AIDA DART asteroid deflection test: planetary

defense and science objectives. Planet. Space Sci. 157, 104–115. https://doi.org/10.1016/j.pss.2018.02.015.

Cheng, A.F., Stickle, A.M., Fahnestock, E.G., Dotto, E., Della Corte, V., Chabot, N.L., Rivkin, A.S., 2020. DART mission determination of momentum transfer: model of ejecta plume observations. Icarus 352, 113989. https://doi.org/10.1016/j.icarus.2020.113989.

Cotto-Figueroa, D., Statler, T.S., Richardson, D.C., Tanga, P., 2015. Coupled spin and shape evolution of small rubble-pile asteroids: self-limitation of the YORP effect. Astrophys. J. 803, 25. https://doi.org/10.1088/0004-637x/803/1/25.

Daly, M.G., Barnouin, O.S., Seabrook, J.A., Roberts, J., Dickinson, C., Walsh, K.J., Jawin, E.R., Palmer, E.E., Gaskell, R., Weirich, J., Haltigin, T., Gaudreau, D., Brunet, C., Cunningham, G., Michel, P., Zhang, Y., Ballouz, R.L., Neumann, G., Perry, M.E., Philpott, L., Al Asad, M.M., Johnson, C.L., Adam, C.D., Leonard, J.M., Geeraert, J.L., Getzandanner, K., Nolan, M.C., Daly, R.T., Bierhaus, E.B., Mazarico, E., Rozitis, B., Ryan, A.J., Dellaguistina, D.N., Rizk, B., Susorney, H.C.M., Enos, H.L., Lauretta, D.S., 2020. Hemispherical differences in the shape and topography of asteroid (101955) bennu. Sci. Adv. 6 https://doi.org/10.1126/sciadv.abd3649.

Ferrari, F., Tanga, P., 2020. The role of fragment shapes in the simulations of asteroids as gravitational aggregates. Icarus 350, 113871. URL: https://www.sciencedirect.com/science/article/pii/S0019103520302517. https://doi.org/10.1016/j.icarus.2020.113871.

Gundlach, B., Blum, J., 2013. A new method to determine the grain size of planetary regolith. Icarus 223, 479–492. https://doi.org/10.1016/j.icarus.2012.11.039.

Harris, A.W., Fahnestock, E.G., Pravec, P., 2009. On the shapes and spins of "rubble pile" asteroids. Icarus 199, 310–318. https://doi.org/10.1016/j.icarus.2008.09.012.

Hartzell, C.M., 2019. Dynamics of 2D electrostatic dust levitation at asteroids. Icarus 333, 234–242. https://doi.org/10.1016/j.icarus.2019.05.013.

Hartzell, C.M., Scheeres, D.J., 2011. The role of cohesive forces in particle launching on the Moon and asteroids. Planet. Space Sci. 59, 1758–1768. https://doi.org/10.1016/j.pss.2011.04.017 lunar Dust, Atmosphere and Plasma: The Next Steps.

Hergenrother, C., Maleszewski, C., Nolan, M., Li, J.Y., d'Aubigny, CH., Shelly, F., Howell, E., Kareta, T., Izawa, M., Barucci, M., et al., 2019. The operational environment and rotational acceleration of asteroid (101955) bennu from osiris-rex observations. Nat. Commun. 10, 1–10. https://doi.org/10.1038/s41467-019-09213-x.

Hestroffer, D., Sánchez, P., Staron, L., Bagatin, A.C., Eggl, S., Losert, W., Murdoch, N., Opsomer, E., Radjai, F., Richardson, D.C., et al., 2019. Small solar system bodies as granular media. Astron. Astrophys. Rev. 27, 6. https://doi.org/10.1007/s00159-019-0117-5.

Hirabayashi, M., 2015. Failure modes and conditions of a cohesive, spherical body due to YORP spin-up. Mon. Not. R. Astron. Soc. 454, 2249–2257. https://doi.org/10.1093/mnras/stv2017.

Hirabayashi, M., Davis, A.B., Fahnestock, E.G., Richardson, D.C., Michel, P., Cheng, A.F., Rivkin, A.S., Scheeres, D.J., Chesley, S.R., Yu, Y., Naidu, S.P., Schwartz, S.R., Benner, L.A., Pravec, P., Stickle, A.M., Jutzi, M., 2019. Assessing possible mutual orbit period change by shape deformation of Didymos after a kinetic impact in the NASA-led double asteroid redirection test. Adv. Space Res. 63, 2515–2534. https://doi.org/10.1016/j.asr.2018.12.041.

Hirabayashi, M., Nakano, R., Tatsumi, E., Walsh, K.J., Barnouin, O.S., Michel, P., Hartzell, C.M., Britt, D.T., Sugita, S., Ichiro Watanabe, S., Bottke, W.F., Scheeres, D. J., Ballouz, R.L., Cho, Y., Morota, T., Howell, E.S., Lauretta, D.S., 2020. Spin-driven evolution of asteroids' top-shapes at fast and slow spins seen from (101955) Bennu and (162173) Ryugu. Icarus 113946. https://doi.org/10.1016/j.icarus.2020.113946.

Holsapple, K.A., 2007. Spin limits of solar system bodies: from the small fast-rotators to 2003 EL61. Icarus 187, 500–509. https://doi.org/10.1016/j.icarus.2006.08.012.

Holsapple, K.A., Michel, P., 2008. Tidal disruptions: II. A continuum theory for solid bodies with strength, with applications to the solar system. Icarus 193, 283–301. https://doi.org/10.1016/j.icarus.2007.09.011.

Hu, S., Richardson, D.C., Zhang, Y., Ji, J., 2021. Critical spin periods of sub-km-sized cohesive rubble-pile asteroids: dependences on material parameters. Mon. Not. R. Astron. Soc. 502 (4), 5277–5291. https://doi.org/10.1093/mnras/stab412.

Jaeger, J.C., Cook, N.G., Zimmerman, R., 2009. Fundamentals of Rock Mechanics. John Wiley & Sons.

Jiang, M., Shen, Z., Thornton, C., 2013. Microscopic contact model of lunar regolith for high efficiency discrete element analyses. Comput. Geotech. 54, 104–116. https://doi.org/10.1016/j.compgeo.2013.07.006.

Jiang, M., Shen, Z., Wang, J., 2015. A novel three-dimensional contact model for granulates incorporating rolling and twisting resistances. Comput. Geotech. 65, 147–163. https://doi.org/10.1016/j.compgeo.2014.12.011.

Jiang, Y., Zhang, Y., Baoyin, H., 2016. Surface motion relative to the irregular celestial bodies. Planet. Space Sci. 127, 33–43. https://doi.org/10.1016/j.pss.2016.04.007.

Koval, G., Roux, J.N., Corfdir, A., Chevoir, F.M.C., 2009. Annular shear of cohesionless granular materials: from the inertial to quasistatic regime. Phys. Rev. E 79, 021306. https://doi.org/10.1103/PhysRevE.79.021306.

Lätzel, M., Luding, S., Herrmann, H.J., 2000. Macroscopic material properties from quasi-static, microscopic simulations of a two-dimensional shear-cell. Granul. Matter 2, 123–135. https://doi.org/10.1007/s100350000048.

Lauretta, D.S., DellaGiustina, D.N., Bennett, C.A., Golish, D.R., Becker, K.J., Balram-Knutson, S.S., Barnouin, O.S., Becker, T.L., Bottke, W.F., Boynton, W.V., et al., 2019. The unexpected surface of asteroid (101955) bennu. Nature 568, 55–60. https://doi.org/10.1038/s41586-019-1033-6.

Leisner, A., Richardson, D., Statler, T., Nichols, W., Zhang, Y., 2020. An extended parameter space study of the effect of cohesion in gravitational aggregates through

spin-up simulations. Planet. Space Sci. 182, 104845. https://doi.org/10.1016/j.pss.2020.104845.

Luding, S., 2005. Anisotropy in cohesive, frictional granular media. J. Phys. Condens. Matter 17, S2623–S2640. https://doi.org/10.1088/0953-8984/17/24/017.

Masson, S., Martinez, J., 2000. Effect of particle mechanical properties on silo flow and stresses from distinct element simulations. Powder Technol. 109, 164–178. https://doi.org/10.1016/S0032-5910(99)00234-X.

Michel, P., Kueppers, M., Sierks, H., Carnelli, I., Cheng, A.F., Mellab, K., Granvik, M., Kestilä, A., Kohout, T., Muinonen, K., Näsilä, A., Penttila, A., Tikka, T., Tortora, P., Ciarletti, V., Hérique, A., Murdoch, N., Asphaug, E., Rivkin, A., Barnouin, O., Bagatin, A.C., Pravec, P., Richardson, D.C., Schwartz, S.R., Tsiganis, K., Ulamec, S., Karatekin, O., 2018. European component of the AIDA mission to a binary asteroid: characterization and interpretation of the impact of the DART mission. Adv. Space Res. 62, 2261–2272. https://doi.org/10.1016/j.asr.2017.12.020 past, Present and Future of Small Body Science and Exploration.

Michel, P., Kueppers, M., The Hera Investigation Team, 2020. The science return of the ESA Hera mission to the binary asteroid Didymos. In: Europlanet Science Congress 2020 Abstracts, pp. EPSC2020–88.

Michikami, T., Nakamura, A.M., Hirata, N., 2010. The shape distribution of boulders on asteroid 25143 Itokawa: comparison with fragments from impact experiments. Icarus 207, 277–284. https://doi.org/10.1016/j.icarus.2009.10.008.

Michikami, T., Honda, C., Miyamoto, H., Hirabayashi, M., Hagermann, A., Irie, T., Nomura, K., Ernst, C.M., Kawamura, M., Sugimoto, K., Tatsumi, E., Morota, T., Hirata, N., Noguchi, T., Cho, Y., Kameda, S., Kouyama, T., Yokota, Y., Noguchi, R., Hayakawa, M., Hirata, N., Honda, R., Matsuoka, M., Sakatani, N., Suzuki, H., Yamada, M., Yoshioka, K., Sawada, H., Hemmi, R., Kikuchi, H., Ogawa, K., ichiro Watanabe, S., Tanaka, S., Yoshikawa, M., Tsuda, Y., Sugita, S., 2019. Boulder size and shape distributions on asteroid ryugu. Icarus 331, 179–191. https://doi.org/10.1016/j.icarus.2019.05.019.

Molerus, O., 1975. Theory of yield of cohesive powders. Powder Technol. 12, 259–275. https://doi.org/10.1016/0032-5910(75)85025-X.

Naidu, S., Benner, L., Brozovic, M., Nolan, M., Ostro, S., Margot, J., Giorgini, J., Hirabayashi, T., Scheeres, D., Pravec, P., Scheirich, P., Magri, C., Jao, J., 2020. Radar observations and a physical model of binary near-earth asteroid 65803 Didymos, target of the DART mission. Icarus 113777. https://doi.org/10.1016/j.icarus.2020.113777.

Ostro, S.J., Margot, J.L., Benner, L.A.M., Giorgini, J.D., Scheeres, D.J., Fahnestock, E.G., Broschart, S.B., Bellerose, J., Nolan, M.C., Magri, C., Pravec, P., Scheirich, P., Rose, R., Jurgens, R.F., De Jong, E.M., Suzuki, S., 2006. Radar imaging of binary near-earth asteroid (66391) 1999 kw4. Science 314, 1276–1280. https://doi.org/10.1126/science.1133622.

Pajola, M., Lucchetti, A., Ivanovski, S., Poggiali, G., Ieva, S., Perna, D., Dotto, E., Corte, D., Cremonese, G., Amoroso, M., Pirrotta, S., Cheng, A., Chabot, N., Rivkin, A., Barnouin, O., Ernst, C., Daly, T., Hirabayashi, M., Asphaug, E., Schwartz, S., 2020. Boulders size-frequency Distribution on binary asteroid (65803) Didymos: Expected results from LICIACube/LEIA and DART/DRACO cameras. In: Europlanet Science Congress 2020 Abstracts, pp. EPSC2020–117.

Pravec, P., Harris, A., 2007. Binary asteroid population: 1. Angular momentum content. Icarus 190, 250–259. https://doi.org/10.1016/j.icarus.2007.02.023.

Pravec, P., Vokrouhlický, D., Polishook, D., Scheeres, D.J., Harris, A.W., Galad, A., Vaduvescu, O., Pozo, F., Barr, A., Longa, P., et al., 2010. Formation of asteroid pairs by rotational fission. Nature 466, 1085–1088. https://doi.org/10.1038/nature09315.

Raducan, S., Davison, T., Collins, G., 2020. The effects of asteroid layering on ejecta mass-velocity distribution and implications for impact momentum transfer. Planet. Space Sci. 180, 104756. https://doi.org/10.1016/j.pss.2019.104756.

Richardson, D.C., Quinn, T., Stadel, J., Lake, G., 2000. Direct large-scale N-body simulations of planetesimal dynamics. Icarus 143, 45–59. https://doi.org/10.1006/icar.1999.6243.

Richardson, D.C., Leinhardt, Z.M., Melosh, H.J., Michel, P., 2002. Gravitational aggregates: Evidence and evolution. In: Bottke, W.F., Cellino, A., Paolicchi, P., Binzel, P.R. (Eds.), Asteroids III. Univ. of Arizona, Tucson, pp. 501–515.

Rubincam, D.P., 2000. Radiative spin-up and spin-down of small asteroids. Icarus 148, 2–11. https://doi.org/10.1006/icar.2000.6485.

Rumpf, H., 1958. Grundlagen und methoden des granulierens. Chem. Ing. Tech. 30, 144–158. https://doi.org/10.1002/cite.330300307.

Rycroft, C., 2009. Voro++: A three-dimensional Voronoi cell library in C++. Technical Report. Lawrence Berkeley National Lab.(LBNL), Berkeley, CA (United States). URL: https://escholarship.org/uc/item/8sf4t5x8.

Sánchez, D.P., Scheeres, D.J., 2012. Dem simulation of rotation-induced reshaping and disruption of rubble-pile asteroids. Icarus 218, 876–894. https://doi.org/10.1016/j.icarus.2012.01.014.

Sánchez, P., Scheeres, D.J., 2014. The strength of regolith and rubble pile asteroids. Meteorit. Planet. Sci. 49, 788–811. https://doi.org/10.1111/maps.12293.

Sánchez, P., Scheeres, D.J., 2016. Disruption patterns of rotating self-gravitating aggregates: a survey on angle of friction and tensile strength. Icarus 271, 453–471. https://doi.org/10.1016/j.icarus.2016.01.016.

Sánchez, P., Scheeres, D.J., 2018. Rotational evolution of self-gravitating aggregates with cores of variable strength. Planet. Space Sci. 157, 39–47. https://doi.org/10.1016/j.pss.2018.04.001.

Scheeres, D., 2007. Rotational fission of contact binary asteroids. Icarus 189, 370–385. https://doi.org/10.1016/j.icarus.2007.02.015.

Scheeres, D., Hartzell, C., Sánchez, P., Swift, M., 2010. Scaling forces to asteroid surfaces: the role of cohesion. Icarus 210, 968–984. https://doi.org/10.1016/j.icarus.2010.07.009.

Scheeres, D.J., McMahon, J.W., French, A.S., Brack, D.N., Chesley, S.R., Farnocchia, D., Takahashi, Y., Leonard, J.M., Geeraert, J., Page, B., et al., 2019. The dynamic geophysical environment of (101955) bennu based on osiris-rex measurements. Nat. Astron. 3, 352–361. https://doi.org/10.1038/s41550-019-0721-3.

Schwartz, S.R., Richardson, D.C., Michel, P., 2012. An implementation of the soft-sphere discrete element method in a high-performance parallel gravity tree-code. Granul. Matter 14, 363–380. https://doi.org/10.1007/s10035-012-0346-z.

Sheng, Y., Lawrence, C.J., Briscoe, B.J., Thornton, C., 2004. Numerical studies of uniaxial powder compaction process by 3D DEM. Eng. Comput. 21, 304–317.

Stadel, J.G., 2001. Cosmological N-body Simulations and their Analysis. Ph.D. thesis. University of Washington, Washington, DC.

Statler, T.S., 2009. Extreme sensitivity of the yorp effect to small-scale topography. Icarus 202, 502–513. https://doi.org/10.1016/j.icarus.2009.03.003.

Thuillet, F., Michel, P., Maurel, C., Ballouz, R.L., Zhang, Y., Richardson, D.C., Biele, J., Tatsumi, E., Sugita, S., 2018. Numerical modeling of lander interaction with a low-gravity asteroid regolith surface - application to mascot on board hayabusa2. Astron. Astrophys. 615, A41. https://doi.org/10.1051/0004-6361/201832779.

Vokrouhlický, D., Nesvorný, D., Bottke, W.F., 2003. The vector alignments of asteroid spins by thermal torques. Nature 425, 147–151. https://doi.org/10.1038/nature01948.

Walsh, K.J., 2018. Rubble pile asteroids. Annu. Rev. Astron. Astrophys. 56, 593–624. https://doi.org/10.1146/annurev-astro-081817-052013.

Walsh, K.J., Jacobson, S.A., 2015. Formation and evolution of binary asteroids. In: Michel, P., DeMeo, F.E., Bottke, W.F. (Eds.), Asteroids IV. Univ. of Arizona Press, pp. 375–393.

Walsh, K.J., Richardson, D.C., Michel, P., 2008. Rotational breakup as the origin of small binary asteroids. Nature 454, 188–191. https://doi.org/10.1038/nature07078.

Walsh, K.J., Jawin, E.R., Ballouz, R.L., Barnouin, O.S., Bierhaus, E.B., Connolly, H.C., Molaro, J., McCoy, T., Delbo, M., Hartzell, C., et al., 2019. Craters, boulders and regolith of (101955) Bennu indicative of an old and dynamic surface. Nat. Geosci. 12, 242–246. https://doi.org/10.1038/s41561-019-0326-6.

Watanabe, S., Hirabayashi, M., Hirata, N., Hirata, N., Noguchi, R., Shimaki, Y., Ikeda, H., Tatsumi, E., Yoshikawa, M., Kikuchi, S., Yabuta, H., Nakamura, T., Tachibana, S., Ishihara, Y., Morota, T., Kitazato, K., Sakatani, N., Matsumoto, K., Wada, K., Senshu, H., Honda, C., Michikami, T., Takeuchi, H., Kouyama, T., Honda, R., Kameda, S., Fuse, T., Miyamoto, H., Komatsu, G., Sugita, S., Okada, T., Namiki, N., Arakawa, M., Ishiguro, M., Abe, M., Gaskell, R., Palmer, E., Barnouin, O.S., Michel, P., French, A.S., McMahon, J.W., Scheeres, D.J., Abell, P.A., Yamamoto, Y., Tanaka, S., Shirai, K., Matsuoka, M., Yamada, M., Yokota, Y., Suzuki, H., Yoshioka, K., Cho, Y., Tanaka, S., Nishikawa, N., Sugiyama, T., Kikuchi, H., Hemmi, R., Yamaguchi, T., Ogawa, N., Ono, G., Mimasu, Y., Yoshikawa, K., Takahashi, T., Takei, Y., Fujii, A., Hirose, C., Iwata, T., Hayakawa, M., Hosoda, S., Mori, O., Sawada, H., Shimada, T., Soldini, S., Yano, H., Tsukizaki, R., Ozaki, M., Iijima, Y., Ogawa, K., Fujimoto, M., Ho, T.M., Moussi, A., Jaumann, R., Bibring, J.P., Krause, C., Terui, F., Saiki, T., Nakazawa, S., Tsuda, Y., 2019. Hayabusa2 arrives at the carbonaceous asteroid 162173 ryugu—a spinning top-shaped rubble pile. Science 364, 268–272. https://doi.org/10.1126/science.aav8032.

Yasin, S.J.M., Tatsuoka, F., 2000. Stress history-dependent deformation characteristics of dense sand in plane strain. Soils Found. 40, 77–98. https://doi.org/10.3208/sandf.40.2_77.

Yu, Y., Michel, P., Hirabayashi, M., Schwartz, S.R., Zhang, Y., Richardson, D.C., Liu, X., 2018. The dynamical complexity of surface mass shedding from a top-shaped asteroid near the critical spin limit. Astron. J. 156, 59. https://doi.org/10.3847/1538-3881/aaccf7.

Zhang, Y., Lin, D.N.C., 2020. Tidal fragmentation as the origin of 1I/2017 U1 ('Oumuamua). Nat. Astron. 4, 852–860. https://doi.org/10.1038/s41550-020-1065-8.

Zhang, Y., Michel, P., 2020. Tidal distortion and disruption of rubble-pile bodies revisited - soft-sphere discrete element analyses. Astron. Astrophys. 640, A102. https://doi.org/10.1051/0004-6361/202037856.

Zhang, Y., Richardson, D.C., Barnouin, O.S., Maurel, C., Michel, P., Schwartz, S.R., Ballouz, R.L., Benner, L.A., Naidu, S.P., Li, J., 2017. Creep stability of the proposed aida mission target 65803 didymos: I. discrete cohesionless granular physics model. Icarus 294, 98–123. https://doi.org/10.1016/j.icarus.2017.04.027.

Zhang, Y., Richardson, D.C., Barnouin, O.S., Michel, P., Schwartz, S.R., Ballouz, R.L., 2018. Rotational failure of rubble-pile bodies: influences of shear and cohesive strengths. Astrophys. J. 857, 15. https://doi.org/10.3847/1538-4357/aab5b2.